Modulation of the cell membrane lipid milieu by peroxisomal β-oxidation induces Rho1 signaling to trigger inflammatory responses

Anu S Nath, Brendon D Parsons, Stephanie Makdissi, Rebecca L Chilvers, Yizhu Mu, Ceileigh M Weaver, Irene Euodia, Katherine A Fitze, Juyang Long, Michal Scur, et al.

Cell Reports

Article

Modulation of the cell membrane lipid milieu by peroxisomal β-oxidation induces Rho1 signaling to trigger inflammatory responses

Graphical abstract

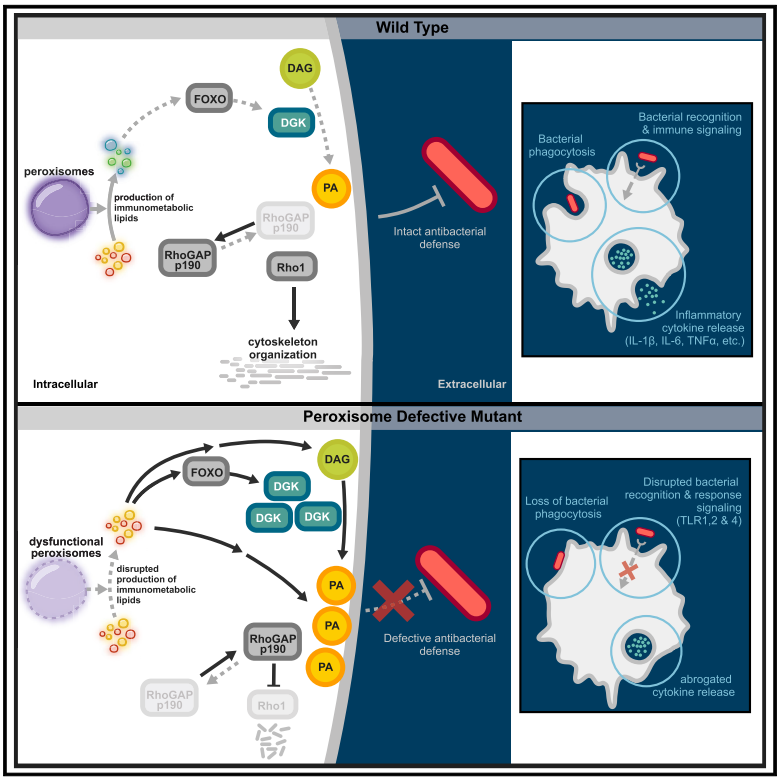

Highlights

- Peroxisomes contribute to changes in the lipid milieu of the plasma membrane
- Peroxisomal β-oxidation modulates Rho1 GTPase-mediated cytokine release by macrophages
- Defective peroxisomal β-oxidation reduces the immune response of macrophages
- Phosphatidic acid levels in immune cells may serve as a marker for autoimmune disorders

Authors

Anu S. Nath, Brendon D. Parsons, Stephanie Makdissi, ..., Yannick Hamon, Richard A. Rachubinski, Francesca Di Cara

Correspondence

dicara@dal.ca

In brief

Immune cells undergo changes in lipid metabolism to mount inflammatory responses. Nath et al. report that peroxisomal β-oxidation influences the lipid milieu of macrophages to activate the Rho1 GTPase-mediated release of inflammatory cytokines. They also show that peroxisomes regulate phosphatidic acid levels, which are reduced in patients with inflammatory disorders.

Nath et al., 2022, Cell Reports *38*, 110433
March 1, 2022
https://doi.org/10.1016/j.celrep.2022.110433

CellPress

Cell Reports

CellPress
OPEN ACCESS

Article

Modulation of the cell membrane lipid milieu by peroxisomal β-oxidation induces Rho1 signaling to trigger inflammatory responses

Anu S. Nath,[1,7] Brendon D. Parsons,[1,7] Stephanie Makdissi,[1] Rebecca L. Chilvers,[1] Yizhu Mu,[1] Ceileigh M. Weaver,[1] Irene Euodia,[1] Katherine A. Fitze,[1] Juyang Long,[1] Michal Scur,[1] Duncan P. Mackenzie,[1] Andrew P. Makrigiannis,[1] Nicolas Pichaud,[2,3] Luc H. Boudreau,[2,3] Andrew J. Simmonds,[4] Christine A. Webber,[4] Beata Derfalvi,[5] Yannick Hamon,[6] Richard A. Rachubinski,[4] and Francesca Di Cara[1,5,8,*]

[1]Dalhousie University, Department of Microbiology and Immunology, Halifax, NS B3K 6R8, Canada
[2]Université de Moncton, Department of Chemistry and Biochemistry, Moncton, NB E1A 3E9, Canada
[3]New Brunswick Centre for Precision Medicine (NBCPM), Moncton, NB E1A 3E9, Canada
[4]University of Alberta, Department of Cell Biology, Edmonton, AB T6G 2H7, Canada
[5]Dalhousie University, Department of Pediatrics, Halifax, NS B3K 6R8, Canada
[6]Aix Marseille Univ, CNRS, INSERM, CIML, Marseille, France
[7]These authors contributed equally
[8]Lead contact
*Correspondence: dicara@dal.ca
https://doi.org/10.1016/j.celrep.2022.110433

SUMMARY

Phagocytosis, signal transduction, and inflammatory responses require changes in lipid metabolism. Peroxisomes have key roles in fatty acid homeostasis and in regulating immune function. We find that *Drosophila* macrophages lacking peroxisomes have perturbed lipid profiles, which reduce host survival after infection. Using lipidomic, transcriptomic, and genetic screens, we determine that peroxisomes contribute to the cell membrane glycerophospholipid composition necessary to induce Rho1-dependent signals, which drive cytoskeletal remodeling during macrophage activation. Loss of peroxisome function increases membrane phosphatidic acid (PA) and recruits RhoGAPp190 during infection, inhibiting Rho1-mediated responses. Peroxisome-glycerophospholipid-Rho1 signaling also controls cytoskeleton remodeling in mouse immune cells. While high levels of PA in cells without peroxisomes inhibit inflammatory phenotypes, large numbers of peroxisomes and low amounts of cell membrane PA are features of immune cells from patients with inflammatory Kawasaki disease and juvenile idiopathic arthritis. Our findings reveal potential metabolic markers and therapeutic targets for immune diseases and metabolic disorders.

INTRODUCTION

Metabolic and immune response pathways are intimately intertwined (Ferrante, 2013; Lee et al., 2018; Musselman et al., 2017; Zmora et al., 2017). Recent evidence has revealed a wider role for metabolic networks during development, activation, and regulation of distinct immune effector functions of different immune cell lineages (Kominsky et al., 2010; O'Neill and Pearce, 2016; Teng et al., 2019; Pearce and Pearce, 2013; Zhang et al., 2017). Lipids in particular have emerged as important factors in immunity. Both innate and adaptive immune cells undergo changes in lipid metabolism in response to infection (Hubler and Kennedy, 2016). For example, macrophage lipid metabolism is rapidly reprogrammed during infection to support an array of immune functions, such as phagocytosis and secretion of proinflammatory cytokines (Hubler and Kennedy, 2016).

The metabolism of fatty acids (FAs) is a major source of biological lipids that form cell membranes and regulate inflammatory processes (Dowds et al., 2014; Hubler and Kennedy, 2016; Sadik and Luster, 2012). FAs are precursors to phospholipids (PLs) such as glycerophospholipids (GLs) and sphingolipids (SLs), triglycerides (TAGs), and eicosanoids, which have pivotal roles in the activation and function of macrophages, invariant natural killer T (iNKT) cells, and other T cells. PLs contribute to the formation of membrane domains where cell receptors mediate signal transduction and regulate membrane trafficking (Levin et al., 2017; O'Donnell et al., 2018; Yang et al., 2018). Dysregulated lipid metabolism may underlie the immune cell dysfunction of immune disorders, as evidenced by the roles of macrophages in atherosclerosis (Di Gioia et al., 2020; Palsson-McDermott and O'Neill, 2020; Remmerie and Scott, 2018). Despite recent recognition of the importance of lipid metabolism in immunity, the regulation of distinct lipid changes in the activation or inhibition of specific pathways in immune cells remains poorly understood.

Peroxisomes are organelles that regulate the synthesis and turnover of complex lipids, including the β-oxidation of very-long chain

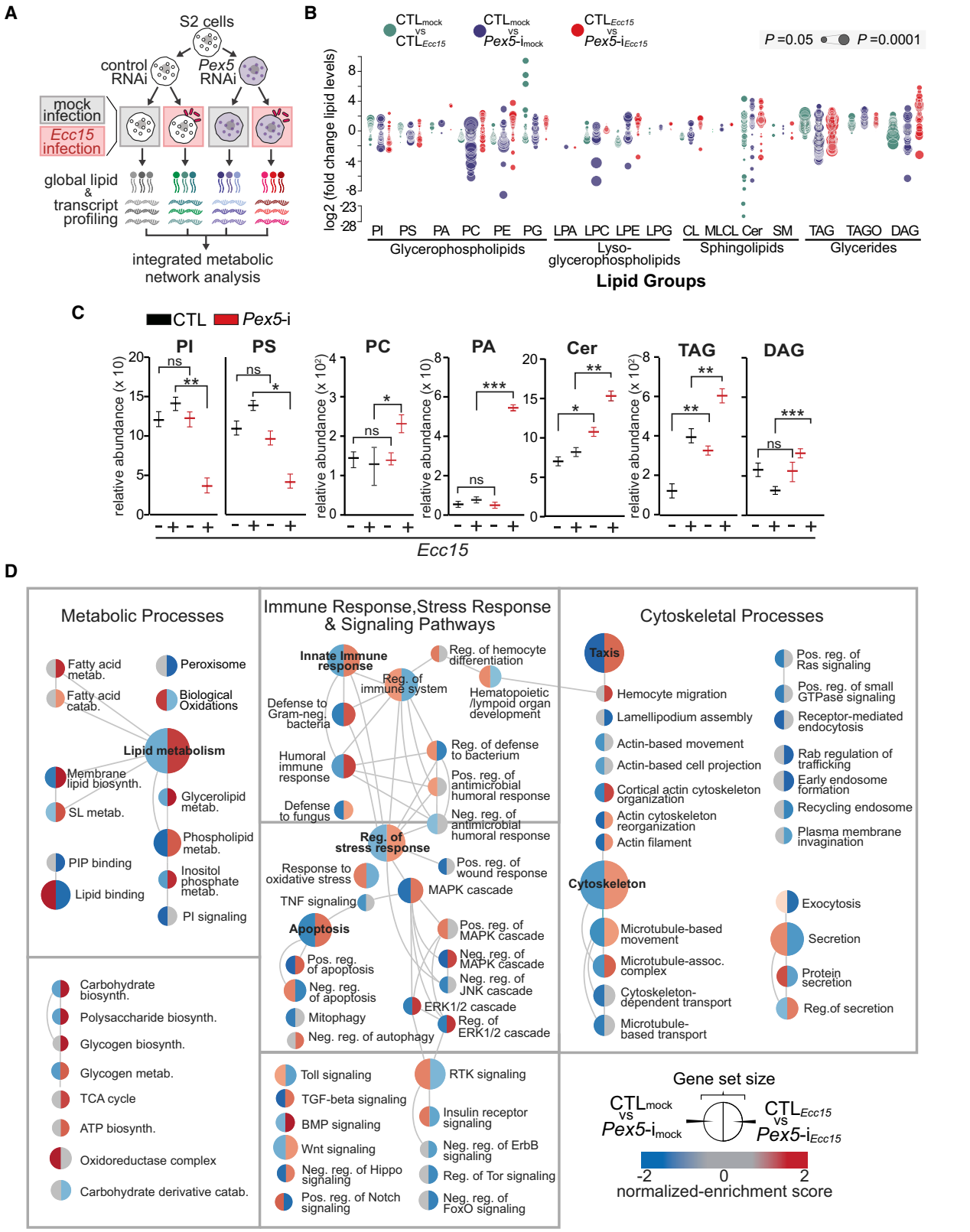

(legend on next page)

FAs, the synthesis of ether lipids, and the α-oxidation of branched chain FAs (Schrader and Fahimi, 2006; Wanders and Waterham, 2006). Previous work has suggested that peroxisomes are pivotal to signaling networks that govern immune cell activation and function in *Drosophila* (Di Cara et al., 2017), mouse (Di Cara et al., 2017; Eguchi et al., 1979; Facciotti et al., 2012; Vijayan et al., 2017), and human (Di Cara et al., 2019a; Dixit et al., 2010; Gilchrist et al., 1974). In particular, previous reports have shown a direct role for peroxisomes in macrophage-mediated phagocytosis (Stroschein-Stevenson et al., 2006; Di Cara et al., 2017), as well as a requirement for peroxisomes in the release of antimicrobial peptides by macrophages in response to bacterial pathogen-associated molecular patterns (Di Cara et al., 2017). Common to these immune responses is the role of the cytoskeleton. Defects in cytoskeleton remodeling impact essential immune events such as inflammatory cytokine secretion and phagocytosis, which ultimately decrease the ability of an animal to survive bacterial infection. These findings led us to hypothesize that cytoskeletal defects observed in peroxisome-deficient cells are due to a breakdown in peroxisome metabolism and that peroxisome-derived lipid metabolites regulate cytoskeleton-mediated immune responses.

We investigated how peroxisome-mediated lipid metabolism influences macrophage function to better understand the metabolic pathways that control immune cell activity. Given the conserved central role for peroxisomes in lipid metabolism across phyla, we investigated how peroxisome lipid metabolism regulates signals that engage inflammatory and immune responses in *Drosophila* plasmatocytes, a cell population considered the fly equivalent of mammalian macrophages (Cherry, 2008; Lemaitre and Hoffmann, 2007; Parsons and Foley, 2016; Rizki and Rizki, 1980). We found that a lack of functional peroxisomes in plasmatocytes altered the amount and cellular distribution of distinct GLs during plasmatocyte immune activation in *Drosophila* and confirmed these findings in murine macrophages. Specifically, we observed that defects in peroxisomal β-oxidation disrupted the lipid milieu necessary for proper cytoskeletal remodeling during bacterial challenge. Given the profound effects of inhibiting these pathways in models of autoimmune disorders, our study regards the peroxisome as an organelle that is unexplored as a therapeutic target for the treatment of immune and infectious diseases.

RESULTS

Changes in the profile of cellular lipids during infection require peroxisome metabolism

To determine whether peroxisome lipid metabolism contributes to signaling pathways during immune defense, we surveyed the global lipid profile of peroxisome-deficient Schneider 2 cells (S2 cells) (Schneider, 1972) during infection. We analyzed S2 cells depleted of *Peroxin5* (*Pex5*-i cells), the receptor required for the import of most proteins into the peroxisomal matrix (Smith and Aitchison, 2013), that have defects in peroxisome biogenesis and function (Di Cara et al., 2019b; Klein et al., 2001) (Figure 1A). We probed the lipid profiles of wild-type S2 cells (CTLs) and *Pex5*-i cells mock-treated or infected with a pathogenic bacterium, *Erwinia corotorova corotorova* (*Ecc15*) (Basset et al., 2000) (Figure 1A). The analysis identified 893 species of the PL and glyceride classes (Figure 1B, Table S1). When the lipid profiles of CTLs exposed to *Ecc15* were compared with those of uninfected CTLs, 79% of the 893 identified lipid species changed in amount (Figure 1B, Table S1). Moreover, 72% and 84% of the 893 lipids identified showed changes in amount when CTLs were compared with *Pex5*-i cells under uninfected or *Ecc15*-infected conditions, respectively (Figure 1B, Table S1). Therefore, S2 cells change their lipid milieu during infection, and some of the changes depend on peroxisomes. Previous studies have reported that cells with dysfunctional peroxisomes have high amounts of glycerides and phosphatidylethanolamines (PEs) with fatty acyl chain lengths of >40 carbon atoms (Herzog et al., 2016). Our screen revealed that *Pex5*-i cells had increased TAGs and PEs with very-long chain FAs (Figure S1A, Table S1), confirming the robustness of this method in identifying lipid changes in cells of the two genotypes.

To identify which changes in lipid species were modulated during infection, we grouped all lipid species identified into classes and compared the lipid profiles of CTLs exposed to *Ecc15* to uninfected CTLs. Our analysis revealed changes in the amounts in the phosphatidylinositol (PI), phosphatidylserine (PS), phosphatidylglycerol (PG), ceramide (Cer), TAG, and diacylglyceride (DAG) classes (Figure 1B).

We next determined which classes of lipids induced during infection changed in amount following depletion of peroxisomal metabolism. We compared the lipid profiles of infected *Pex5*-i cells to infected CTLs. The overall comparison illustrated in the bubble graphs (Figure 1B) showed changes in the amounts of lipid classes that are key components of the plasma membrane and involved in cellular signaling, i.e., GLs such as PA, phosphatidylcholine (PC) and PI, sphingolipids (SLs) such as Cer, and glycerides such as DAG. Notably, these lipids were either unchanged or changed in a different direction and/or to a different degree when we compared the profiles of uninfected *Pex5*-i cells and CTLs (Figures 1B and 1C), suggesting that peroxisomal metabolism participates in defining the distinct lipid milieu of infected cells.

Plotting the abundance of each lipid class normalized to the abundance of internal standards in all sample groups, we found

Figure 1. Systems biology analyses show peroxisome-dependent contributions to metabolic and cellular signaling during bacterial infection

(A) Schematic for peroxisome-dependent lipids and RNA-seq-based changes in gene expression during infection.

(B) Lipidomic analysis of control S2 cells (CTL) in mock-treated versus *Ecc15*-infected conditions, mock-treated CTLs versus *Pex5*-i cells, and infected CTLs versus infected *Pex5*-i cells. Values are shown as relative log2 fold-changes. Lipidomics data were from four independent experiments and are represented as means. Each dot represents a lipid species. Dot size indicates statistical significance.

(C) Comparison of the ratios between the abundance of a chosen lipid species and the abundance of internal lipid standards. Data are from four independent experiments and are shown as means ± SD. Significance was determined using Student's *t* test. ***p < 0.001; **p < 0.01; *p < 0.05; ns, not significant.

(D) Gene interaction network of KEGG terms positively or negatively enriched in *Pex5*-i cells relative to CTLs mock-treated (right side of circle) or infected (left side of circle). Red and blue indicate positive and negative KEGG terms, respectively. Color intensity indicates degree of enrichment. See also Figure S1.

that during infection, CTLs have increased amounts of PI and PS, while *Pex5*-i cells showed decreases in PI and PS and increases in PC, PA, Cer, TAG, and DAG (Figure 1C). We calculated *Z* scores for all 893 identified lipids to establish thresholds of significance for the lipid species reported in Figure 1B that accumulated or decreased in a peroxisome-dependent manner during infection. Our *Z* scores showed that all lipid species belonging to the PA and PG lipid classes were elevated in infected *Pex5*-i cells compared with infected CTLs, with PA (36:2), PC (26:2), and PG (30:0 and 32:0) among the most significantly elevated lipid species (Figures S1B and S1C). In contrast, nearly all PI and PS lipid species were lower in amount in infected *Pex5*-i cells compared with infected CTLs, with PI (34:6) and PS (36:2) among the most significantly reduced lipid species (Figures S1B and S1D).

Our findings suggest that peroxisome function is important to generate a specific cellular milieu of lipids that supports cellular responses to infection.

Peroxisomes support metabolic responses to mediate immune signaling

To determine the metabolic signaling that supports immune pathway activation in response to microbial infection, we carried out genome-wide transcriptional profiling of CTLs and *Pex5*-i cells either mock-treated or *Ecc15*-infected cells. We identified 327 genes upregulated and 389 genes downregulated ($p < 0.05$) in mock-treated *Pex5*-i cells compared with CTLs, and 393 genes upregulated and 353 genes downregulated ($p < 0.05$) in *Ecc15*-infected *Pex5*-i cells compared with *Ecc15*-infected CTLs (Table S2). Gene network analysis of the processes and pathways enriched from differentially expressed genes of infected *Pex5*-i cells compared with infected CTLs were overrepresented among gene sets belonging to lipid metabolic processes, including the metabolism of FAs, membrane lipids, and phospholipids, as well as other metabolic processes such as carbohydrate and polysaccharide biosynthesis (Figure 1D). These data are in agreement with the findings of a study that found increased carbohydrate and purine metabolism in response to peroxisome dysfunction in *Drosophila* and mouse (Wangler et al., 2017), and some components of these pathways were also enriched when CTLs were compared with uninfected *Pex5*-i cells (Figure 1D). Other genes were strongly enriched in the master cellular regulatory signaling of immunity (e.g., regulators of stress response pathways and innate immune response pathways), growth control cell signaling pathways (e.g., Tor pathway, Hippo signaling), and cytoskeleton remodeling (e.g., Rho GTPases) (Figure 1D, Table S2). These results suggest that peroxisomes are required for regulation of phospholipid metabolic pathways, immune pathways, stress response pathways, and cytoskeleton remodeling during infection (Figure 1D). Indeed, these functions were either not enriched or differentially enriched when we compared the gene expression profiles of mock-treated *Pex5*-i cells to those of CTLs (Figure 1D). In particular, lipid metabolic genes and stress response signaling genes were differentially enriched between mock-treated and *Ecc15*-infected conditions. Cytoskeleton regulatory genes were negatively enriched between uninfected cells of the two genotypes, while they were positively enriched during infection. Of the 2,514 genes upregulated in infected CTLs versus uninfected CTLs, 1,232 were downregulated (505 genes) or unchanged (727 genes) in infected *Pex5*-i cells compared with infected CTLs. Of the 1,610 genes downregulated in infected versus uninfected CTL cells, 179 genes were instead upregulated in infected *Pex5*-i cells (Figure S1E). Pearson correlation analysis identified transcript changes in *Pex5*-i cells that negatively correlated to profiles observed in CTLs during infection (Figure S1F). In this group, we identified genes that are involved in GL metabolism (Figure S1G), reinforcing data from the lipidomic analysis showing that depletion of peroxisome activity impacts the GL milieu required during infection.

Pex1 mutant S2 cells show metabolic and immune defects observed in *Pex5*-i cells

To verify that the changes in lipid metabolic pathways observed in infected *Pex5*-i cells were not the result of *Pex5* mutation per se but were the result of overall peroxisomal dysfunction, we made a CRISPR/Cas9 mutant S2 cell line (Bassett et al., 2014) deleted for the *Peroxin1* (*Pex1*) gene. *Pex1* codes for a member of the AAA-family of ATPases and mediates protein import into peroxisomes through its recycling of the Pex5 receptor (Smith and Aitchison, 2013). Mutation of *Pex1* renders peroxisomes nonfunctional (Mast et al., 2011; Walter et al., 2001). The *Pex1* mutant cell line (*Pex1* cells) does not express *Pex1* mRNA (Figure S2A). GFP fused to the peroxisome targeting signal type 1 (PTS1) serine-lysine-leucine-CO_2H (GFP-SKL) labeled peroxisomes in CTLs and *Pex1* cells. *Pex1* cells showed defects in peroxisome protein import, since GFP-SKL was cytosolic in these cells (Figure S2B). Peroxisome protein import was rescued when we transfected *Pex1* cells with wild-type (WT) *Pex1* cDNA as shown by GFP-SKL localization to puncta characteristic of peroxisomes (Figure S2B). *Pex5*-i cells exhibit defects of the cortical actin cytoskeleton in S2 cells and *Drosophila* primary immune cells (Di Cara et al., 2017). *Pex1* cells also showed defects in cortical actin organization (Figure S2B). Expression of WT *Pex1* cDNA in *Pex1* cells restored actin organization (Figure S2B) and cell area (Figure S2C), whose extent is dependent on the organization of the cytoskeleton, to what was observed in CTLs (Figures S2B and S2C).

CTLs infected with *Ecc15* showed increased expression of the antimicrobial peptide gene *Dpt* (Figure 2A) (Basset et al., 2000), while infected *Pex1* cells showed no induction of *Dpt* expression, confirming the peroxisome requirement for immune signaling activation (Di Cara et al., 2017). Moreover, flow cytometry (FC) showed that the uptake of *E. coli* by *Pex1* cells was reduced compared with CTLs (Figure S2D).

Transcriptional analysis identified significant dysregulation of key phospholipid metabolic pathway enzymes in *Pex1* cells during infection (Figure 2A), as was also observed in the transcriptomic analysis of *Pex5*-i cells (Figure S1G). Specifically, phosphatidylserine synthase (*CG4825*) (Valadas et al., 2018), phosphatidylinositol synthase (*Pis*) (Laurinyecz et al., 2016), CDP-diacylglycerol synthase (*CdsA*) (Volta et al., 1999), diacylglycerol kinase (*DGK*) (Wightman et al., 2012), and *Lipin* (Schmitt et al., 2015) were dysregulated in infected *Pex1* cells (Figures 2A and 2B). Additionally, we assayed the gene expression levels of key enzymes of the sphingolipid metabolic pathway, such as

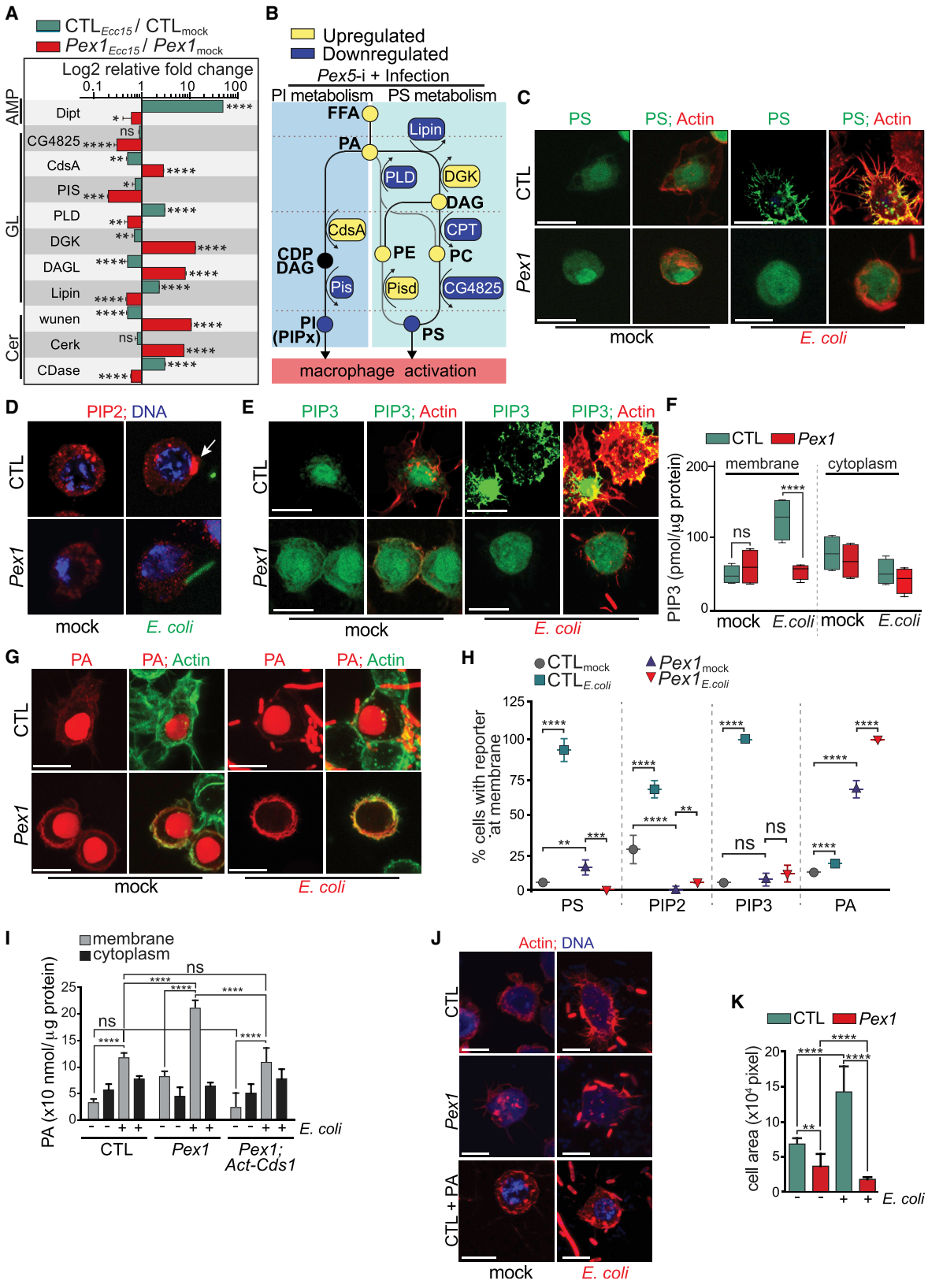

(legend on next page)

ceramidase (*CDase*) (Yuan et al., 2011), which converts ceramides (Cer) to complex sphingolipids (Acharya and Acharya, 2005), and ceramide kinase (*Cerk*) (Dasgupta et al., 2009), which catalyzes the phosphorylation of Cer to Cer-1p, and observed that these genes were differentially expressed in infected *Pex1* cells compared with infected CTLs (Figure 2A). Together, these data demonstrate that *Pex1* cells mirror infected *Pex5*-i cells in their altered expression of phospholipid metabolic genes. Because *Pex1* showed greater phenotypic expressivity and penetrance than the RNAi-mediated *Pex5* depletion, we used *Pex1* cells for all subsequent investigations.

Peroxisome depletion affects the amounts and distributions of distinct glycerophospholipids

Our lipidomic and transcriptomic analyses indicated that peroxisomes regulate the GL milieu during infection. We have reported that peroxisome-depleted cells show cortical actin cytoskeleton defects (Di Cara et al., 2017). GLs are key components of the cell membrane, and their localization to distinct membranes in macrophages promotes cytoskeleton remodeling that supports responses to immune stimuli. Upon infection, PIs, i.e., $PI(4,5)P_2$ (PIP2), and $PI(3,4,5)P_3$ (PIP3), and PS accumulate at the cell membrane, where they support the assembly of mediators of immune cell activation (Aderem and Underhill, 1999; Burkhardt, 2013; Flannagan et al., 2012; Lacy and Stow, 2011; Murray and Stow, 2014; O'Donnell et al., 2018). PIs and PS decreased, while their precursors PA and DAG increased in cells lacking functional peroxisomes relative to CTLs during infection (Figure 2B). To determine whether lack of peroxisome function affects the distribution of these deregulated GLs, we monitored the distribution of PS, PIP2, and PIP3 in uninfected and infected CTLs and *Pex1* cells. We visualized the distribution of PIP2 by immunofluorescence (IF) labeling, and PIP3 and PS by the fluorescent reporters GRP1-GFP and GFP-Lact-C2, respectively (Khuong et al., 2010; Lai et al., 2013; Yeung et al., 2008). In unchallenged conditions, PS, PIP2, and PIP3 were diffuse in the cytoplasm of CTLs and *Pex1* cells, both of which showed the typically round profiles of unchallenged cells (Figures 2C–2E). PS was found in the cytoplasm of infected *Pex1* cells, but localized to cell membrane protrusions in infected CTLs (Figure 2C). In infected CTLs, PIP2 staining was stronger in intensity than in infected *Pex1* cells and was seen to concentrate in spots at the cell edge (Figure 2D). PIP3 localized to cell membrane protrusions in infected CTLs but was restricted to the cytoplasm in infected *Pex1* cells (Figure 2E).

PIs are important signaling molecules, and synthesis of PIs such as PIP3 has been linked to peroxisome metabolism (Jeynov et al., 2006). We measured PIP3 amounts in membrane and cytoplasmic fractions of CTLs and *Pex1* cells and confirmed increased amounts of PIP3 in infected CTLs versus uninfected CTLs, and that the amounts of PIP3 in *Pex1* cell membranes did not change in the presence or absence of *E. coli* (Figure 2F). Differences in PIP3 amounts were not large between the cytoplasmic fractions of cells of both genotypes and under both conditions. Live imaging of CTLs and *Pex1* cells was used to examine the dynamics of PIP3 reporter distribution to the cell membrane protrusions 30–60 min after infection. The PIP3 reporter dynamically distributed to the sites where membrane protrusions formed in infected CTLs (Video S1). In contrast, infected *Pex1* cells did not form protrusions, and the PIP3 reporter remained in the cytoplasm of the still round cell (Video S2).

PA accumulates at the cell membrane in *Pex1* cells and causes cortical cytoskeleton defects

Lipidomic analysis of *Pex5*-i cells suggested that cells with defective peroxisomes accumulate PA and that defects associated with this accumulation are exacerbated by infection (Figures 1C, S1B, and S1C). We visualized the cellular distribution of PA by monitoring the location of a fluorescent PA reporter, PABD-RFP. In uninfected CTLs, PABD-RFP was found mainly in the nucleus, while in *Pex1* cells PABD-RFP was also visible at the cell membrane (Figure 2G). Nuclear localization of PABD reporters has been reported for cells lacking PA at the plasma membrane (Nakanishi et al., 2004). Infected *Pex1* cells showed a uniform distribution of PABD-RFP at the cell membrane, which was not observed in infected CTLs (Figure 2G). Live imaging of CTLs and *Pex1* cells was done to examine the dynamics of PABD-RFP distribution 30–60 min after infection with *E. coli*. PABD-RFP accumulated in the nucleus and cytoplasm but was not visible at membrane protrusions of infected CTLs (Video S3). In contrast, PABD-RFP localized to cell membrane protrusions in infected *Pex1* cells (Video S4). Quantification of the fluorescence intensity of reporters at

Figure 2. Peroxisomes contribute to changes in glycerophospholipids during cell infection

(A) Quantification of relative gene expression in CTLs and *Pex1* cells after infection with *Ecc15*. Gene expression is reported for infected CTLs and *Pex1* cells compared with the corresponding gene in mock-treated CTLs and *Pex5*-i cells, respectively.

(B) Pathway of selected metabolic steps in PI and PS metabolism. Boxes indicate genes upregulated (green) or downregulated (red) in infected *Pex5*-i cells compared with infected CTLs. Circles represent metabolites of the pathways that were accumulated (green), reduced (red), or undetected (black) in the lipidomic screen during infection.

(C) Imaging of the Lac2-GFP reporter that detects PS. Green, PS reporter; red, actin; red rods, *E. coli*. Bar, 10 μm.

(D) IF microscopy of PIP2. Red, PIP2; blue, DNA; green rods, *E. coli*. Arrowhead points to a concentration of PIP2. Bar, 10 μm.

(E) Imaging of the GRP1-GFP reporter to detect cellular PIP3. Green, PIP3 reporter; red, actin; red rods, *E. coli*. Bar, 10 μm.

(F) Quantification of PIP3.

(G) Imaging of PA reporter, PABD-RFP. Red, PA reporter; green, actin; red rods, *E. coli*.

(H) Graphic reporting the percentage of cells with a specific lipid localized at the membrane under uninfected and infected conditions.

(I) Quantification of PA in cytoplasmic and cell membrane fractions of cells of the indicated genotypes and conditions.

(J) Actin staining in cells of the indicated genotypes and under the indicated treatments. Blue, DNA; red rods, *E.* coli; red, actin. Bar, 10 μm.

(K) Histogram reporting the area of cells of the indicated genotypes and under the indicated conditions. Values in (H), (I), and (K) report the means ± SD of three independent experiments totaling 30 cells. Significance was determined using a two-way ANOVA test. ****$p < 0.0001$; **$p < 0.01$; *$p < 0.05$; ns, not significant. See also Figure S2 and Videos S1–S4.

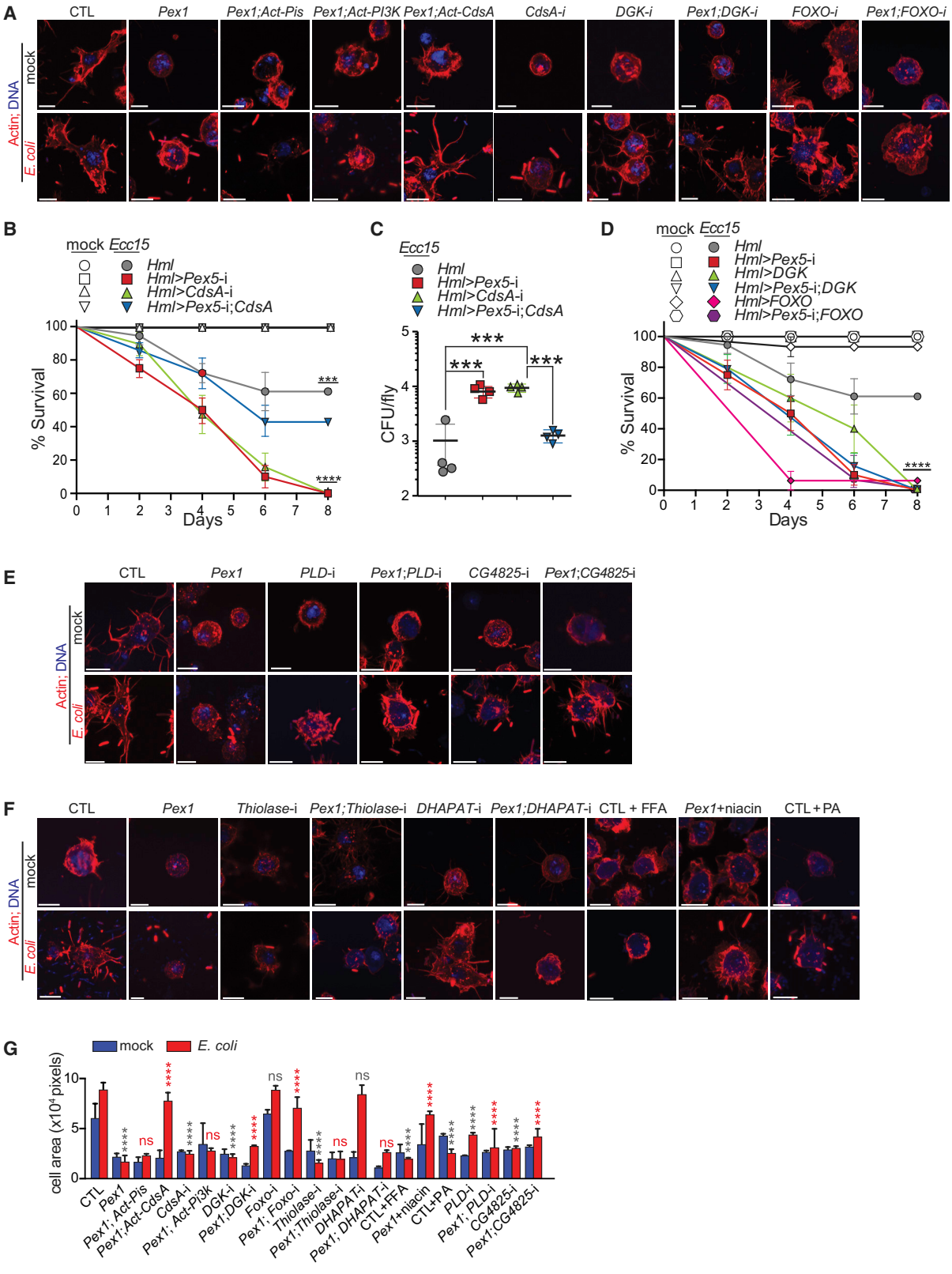

(legend on next page)

the edge/protrusions of cells and in the cytoplasm of cells of both genotypes and under uninfected and infected conditions confirmed that PS, PIP2, and PIP3 were in the cytoplasm of uninfected cells of both genotypes, and in the membrane of CTLs, but not *Pex1* cells, during infection (Figure 2H). In contrast, PABD-RFP localized mainly to the cell membrane in *Pex1* cells, especially during infection (Figure 2H).

We measured PA amounts in membrane and cytoplasm fractions from both CTLs and *Pex1* cells under uninfected and infected conditions. We found more PA in the membrane fraction of uninfected *Pex1* cells compared with that of uninfected CTLs, and the increase in PA at the cell membrane was larger in *Pex1* cells than in CTLs under infection (Figure 2I). Infected CTLs treated with PA did not show a clear cortical actin network and did not form protrusions, in contrast to what was observed in infected *Pex1* cells in the absence or presence of added PA (Figures 2J and 2K).

We performed genetic interaction studies in S2 cells to discriminate whether the cytoskeleton defects observed in *Pex1* cells were caused mainly by the accumulation of PA or by low amounts of PI. We tested if enzymes responsible for the biosynthesis of PI influenced peroxisome-dependent actin remodeling during infection. Overexpression (OE) of the *Pis* gene coding for the enzyme involved in the last step of PI synthesis did not rescue the defects in cortical cytoskeleton organization of infected *Pex1* cells (Figure 3A). Cytoskeleton remodeling-signaling is controlled by PIP3, which is produced by the phosphorylation of PIP2 by class I phosphoinositide 3-kinases (PI 3-kinases) (Deane and Fruman, 2004; Heo et al., 2006; Juss et al., 2012; Reversi et al., 2014). We overexpressed the *PI3K92E* gene encoding PI3-kinase92E in *Pex1* cells to see if it could rescue the cortical cytoskeleton defects observed during infection, but OE of *PI3K92E* did not rescue these defects (Figure 3A). We then overexpressed the *CdsA* gene coding for the enzyme that converts PA to CDP-DAG, the substrate of Pis and an intermediate in the synthesis of other GLs through the cytidine diphosphate diacylglycerol pathway (Volta et al., 1999), in *Pex1* cells. We observed that OE of *CdsA* rescued the defects in actin organization and membrane protrusions of infected *Pex1* cells (Figure 3A). Moreover, when we depleted infected cells of *CdsA*, *CdsA*-i cells showed defects similar to those observed in *Pex1* cells, including abnormal organization of the cortical cytoskeleton and failure of the cells to form membrane protrusions in response to infection (Figure 3A). Additionally, OE of *CdsA* in *Pex1* cells restored the amounts of PA in the membrane to CTL levels (Figure 2I). *CdsA*-i cells showed reduced engulfment of bacteria (Figure S2D), confirming that the defects in the PA metabolic pathway impact cortical cytoskeleton remodeling, thereby affecting immune cell activity. *Pex1*;*CdsA*-i cells showed reduced phagocytosis compared with *Pex1* cells (Figure S2D), supporting the idea that peroxisome activity acts upstream of CdsA in GL metabolism.

To explore the immune requirement for CdsA during infection *in vivo*, we modulated *CdsA* expression in plasmatocytes (*Drosophila* adult macrophages) during septic infection of flies. Adult flies with a targeted depletion of plasmatocyte *CdsA* (*Hml* > *CdsA*-i) had problems surviving septic infection with *Ecc15*. Similar to *Hml* > *Pex5*-i flies, 50% of the *Hml* > *CdsA*-i flies died 4 days after infection, and 100% died after 8 days (Figure 3B). In addition, OE of *CdsA* in *Hml* > *Pex5*-i plasmatocytes (*Hml* > *Pex5*-i;*CdsA*) improved the survival of *Hml* > *Pex5*-i flies to septic infection (Figure 3B). Colony forming unit (CFU) analysis showed that *Hml* > *CdsA*-i flies had a higher bacterial load during septic infection than *Hml* > *UAS-GFP* (*Hml*) control flies and a load similar to that of *Hml* > *Pex5*-i flies (Figure 3C). Notably, *Hml* > *Pex5*-i;*CdsA* flies had a lower bacterial load than *Hml* > *Pex5*-i flies during infection (Figure 3C). Together, these data show that expression of *CdsA* in *Pex1* cells reduces PA levels at the cell membrane and rescues cortical cytoskeleton organization and survival of *Hml* > *Pex5*-i flies after infection.

FOXO responds to peroxisome depletion and contributes to DGK-mediated synthesis of PA in *Pex1* cells

PA is synthesized from DAG by DGK (Figure 2B). We depleted *DGK* in S2 cells (*DGK*-i) and assessed their cortical actin cytoskeleton organization upon infection. Uninfected *DGK*-i cells showed reduced cortical cytoskeleton organization and membrane protrusion formation to the extent observed in uninfected *Pex1* cells (Figure 3A). In contrast, infected *DGK*-i cells showed modest cytoskeleton defects that were not as severe as those of infected *Pex1* cells (Figure 3A). However, depletion of *DGK* in *Pex1* cells (*Pex1*;*DGK*-i cells) rescued the defects in cytoskeleton organization and protrusion formation of infected *Pex1* cells (Figure 3A). These data suggest that a metabolic shift toward an enhanced conversion of DAG to PA and/or an accumulation of PA in *Pex1* cells affects cytoskeleton remodeling (Figure 3A).

DGK expression was upregulated in both *Pex5*-i and *Pex1* cells during infection (Figures 2A and 2B; Figure S1H). In mammals, *DGK* transcription is mediated by the Forkhead box class O (FOXO) transcription factors (Akasaki et al., 2014; Battiprolu et al., 2012; Gross et al., 2008), and FOXO transcription binding

Figure 3. Defects in peroxisomal β-oxidation affect cytoskeleton remodeling and reduce host survival during bacterial infection

(A) Actin staining of cells of the indicated genotypes. Blue, DNA; red, actin; red rods, *E. coli*. Bar, 10 μm.

(B) Survival of *Hml* > *UAS-GFP* control (*Hml*), *Hml* > *Pex5*-i, *Hml* > *CdsA*-I, and *Hml* > *Pex5*-i;*CdsA* flies injected with vehicle or *Ecc15*.

(C) Quantification of pathogen load as measured by CFUs formed by *Ecc15*.

(D) Survival of *Hml* > *UAS-GFP* (*Hml*) control, *Hml* > *Pex5*-i, *Hml* > *DGK*, *Hml* > *Pex5*-i; *DGK*, *Hml* > *FOXO*, and *Hml* > *Pex5*-i;*FOXO* flies injected with vehicle or *Ecc15*.

(E and F) Actin staining of cells of the indicated genotypes. Blue, DNA; red, actin; red rods, *E. coli*. Bar, 10 μm.

(G) Histogram reporting area of cells of the indicated genotypes and under the indicated treatment. Values reported are for 400 flies per genotype and condition in (B) and (D) and for 30 cells in (G). Values reported are the means ± SD of four independent experiments in (B)–(D), and three independent experiments in (G). Significance was determined using the Kaplan Meier and log rank test in (B) and (D), a one-way ANOVA test in (C), and a two-way ANOVA test in (G). ****$p < 0.0001$; ***$p < 0.001$; ns, not significant. Black asterisks, significance compared with CTLs. Red asterisks, significance compared with *Pex1* cells. See also Figures S1 and S2.

sites have been identified in the promoters of *DGK* genes across phyla, including the Arthropoda that contains *Drosophila* (Webb et al., 2016). FOXO is a regulator of metabolism and innate immunity in *Drosophila* and mammals (Becker et al., 2010; Fink et al., 2016; Cabrera-Ortega et al., 2017; Dionne et al., 2006; Molaei et al., 2019; Seiler et al., 2013). FOXO signaling is enriched in our transcriptomic analysis (Figure 1D), and *FOXO* gene expression is upregulated in *Pex5*-i cells compared with CTLs during infection (Table S2). We asked whether metabolic and immune cues in cells lacking functional peroxisomes might trigger FOXO-mediated upregulation of *DGK* expression leading to the accumulation of PA. Depletion of *FOXO* in *Pex1* cells (*Pex1*;*FOXO*-i cells) partially rescued the cortical cytoskeleton and membrane protrusion defects of infected *Pex1* cells (Figure 3A). Moreover, *FOXO* depletion in *Pex1* cells also rescued the upregulation of *DGK* expression observed during infection of *Pex1* cells (Figure S2E). FOXO localized in the cytoplasm of uninfected CTLs and *Pex1* cells. FOXO was at the limit of detection in the nucleus in infected CTLs but was mostly nuclear in infected *Pex1* cells (Figures S2F and S2G).

To explore the effects of DGK and FOXO on host response to infection *in vivo*, we modulated *DGK* or *FOXO* expression in plasmatocytes during septic infection of flies. Adult flies with targeted OE of *DGK* (*Hml* > *DGK*) or *FOXO* (*Hml* > *FOXO*) in plasmatocytes had reduced capacity to fight septic infection than control *Hml* > *UAS-GFP* (*Hml*) flies (Figure 3D). Similar to *Hml* > *Pex5*-i flies, 40%–50% of *Hml* > *DGK* flies and 90% of *Hml* > *FOXO* flies died 4 days after infection, and 100% died after 8 days (Figure 3D). Additionally, OE of *DGK* (*Hml* > *Pex5*-i; *DGK*) or *FOXO* (*Hml* > *Pex5*-i;*FOXO*) in *Hml* > *Pex5*-i plasmatocytes caused lethality of flies to septic infection at the same rate as for *Hml* > *Pex5*-i flies (Figure 3D). Together, these data suggest that FOXO responds to signaling driven by a depletion in peroxisomes during infection and contributes to the upregulation of *DGK* expression. Increased DGK amounts lead to PA accumulation in infected cells depleted for peroxisomes, triggering cytoskeleton defects that are detrimental to the host's capacity to survive systemic bacterial infections.

Depletion of PS synthetic pathways also contributes to cytoskeleton defects in *Pex1* cells

PA can also be synthesized from PC/PE by phospholipase D (PLD), which is part of the PS synthetic pathway (Miller et al., 1993) (Figure 2B). We generated *PLD*-i S2 cells and assessed the organization of the cortical actin cytoskeleton upon infection. Uninfected *PLD*-i cells exhibited reduced organization in the cortical cytoskeleton and reduced formation of membrane protrusions to the extent observed in uninfected *Pex1* cells (Figure 3E). We also tested *CG4825*-i cells that are depleted for PS synthase (CG4825), the enzyme that produces PS from PC and DAG. *CG4825*-i cells exhibited defects in cortical cytoskeleton organization similar to those observed in *Pex1* cells (Figure 3E). *Pex1*;*CG4825*-i cells showed defects in cortical cytoskeleton organization similar to those observed in *Pex1* cells and *CG4825*-i cells (Figure 3E). Thus, peroxisome-dependent accumulation of PA and reduced amounts of its metabolic products, PI and PS, impact immune cell cytoskeleton remodeling that in turn affects cellular responses to infection *in vitro* and *in vivo*.

Peroxisomal β-oxidation contributes to the cellular lipid metabolic response to infection

Peroxisomal β-oxidation contributes to GL synthesis (Guo et al., 2007; Herzog et al., 2016; Lodhi and Semenkovich, 2014). Therefore, we tested whether actin cytoskeletal remodeling in response to infection relies on GL metabolic inputs from peroxisomal β-oxidation. *Thiolase*-i cells depleted of the peroxisomal β-oxidation enzyme, thiolase (Faust et al., 2012), did not exhibit membrane protrusions when infected (Figure 3F). Infected *Pex1* cells depleted of thiolase (*Pex1*;*Thiolase*-i) showed defects in the cortical cytoskeleton like those in infected *Pex1* cells (Figure 3F). *DHAPAT*-i cells depleted of dihydroxyacetonephosphate acyltransferase (DHAPAT), an enzyme that catalyzes the first step of ether lipid synthesis that occurs only in peroxisomes, were unaffected in cytoskeleton remodeling or membrane protrusion formation during infection (Figure 3F). Moreover, DHAPAT depletion in uninfected or infected *Pex1* cells (*Pex1*;*DHAPAT*-i cells) did not enhance or suppress the defects observed in *Pex1* cells (Figure 3F). Disruptions in peroxisomal β-oxidation lead to increased levels of free fatty acids (FFAs) (Sellin et al., 2018), which can induce the formation of DAGs and TAGs (Lam et al., 2003). Infected *Pex5*-i cells accumulated DAG and TAG and exhibited elevated production of PA from DAG. To determine if defects in cellular responses to bacteria were due in part to excess FFAs, we treated S2 cells for 24 h with an FFA cocktail and observed cortical cytoskeleton defects in treated cells during infection similar to those observed in CTLs treated with PA (Figure 3F). Moreover, cytoskeleton defects were partially rescued when *Pex1* cells were treated prior to infection with niacin, an analog of vitamin B3, which has been shown to reduce the amounts of FFAs in mammals and flies (Di Cara et al., 2018; Nelson et al., 2012) (Figure 3F). Interestingly, the upregulation of *DGK* expression in infected *Pex1* cells pretreated with niacin was rescued to the level observed in infected CTLs (Figure S2E). Quantification of the area of cells of each genotype and under each condition (Figure 3G) confirmed the microscopic observations.

In agreement with these data, flies globally disrupted for peroxisome function (*ubi* > *Pex5*-i) had higher levels of FFAs relative to controls (Figure S2H). Feeding CTL flies and *ubi* > *Pex5*-i flies niacin for 15 days reduced the FFA levels of *ubi* > *Pex5*-i flies to the FFA levels of control flies (Figure S2H). We next tested the survival of *ubi* > *Pex5*-i flies treated with niacin to infection with *Ecc15*. While *ubi* > *Pex5*-i flies died 3 days after infection, those given an oral treatment of niacin for 15 days prior to infection showed a 30% increase in survival on day 3 post-infection relative to untreated *ubi* > *Pex5*-i flies (Figure S2I). Thus, peroxisomal β-oxidation contributes to the lipid cellular changes necessary for the remodeling of the cytoskeleton during the activation of immune cells during infection and impacts the ability of the host to survive systemic infection *in vivo*.

Defects in peroxisomal metabolism but not mitochondrial metabolism result in cytoskeleton defects in S2 cells

Mitochondria and peroxisomes collaborate to maintain cellular lipid homeostasis. Damage to one organelle may affect the metabolic activities of the other. Thus, we tested mitochondrial metabolism in CTLs and *Pex1* cells before and after bacterial

infection. Respiration rates were significantly higher in *Pex1* cells than CTLs (all $p < 0.001$; Figure S3A). However, when respiration rates were normalized to complex IV maximal capacity, which is considered a good marker for mitochondrial content, no significant differences were detected between *Pex1* cells and CTLs (Table S3). These results suggest that both CTLs and *Pex1* cells exhibit similar mitochondrial efficiency and that the differences observed between them are likely due to a difference in mitochondrial content. Therefore, we perturbed the mitochondrial respiratory chain and mitochondrial Krebs cycle by depleting the gene *ND75* encoding the NADH dehydrogenase 75 kDa subunit and the gene *CG3861* encoding citrate synthase in *Pex1* cells. Cortical cytoskeleton defects and reduced numbers of membrane protrusions were not rescued in either *ND75*-i cells or *citrate synthase*-i cells when infected with *E. coli* (Figure S3B), suggesting that the cytoskeleton defects observed in *Pex1* cells during infection are not caused by increased mitochondrial metabolic activity. Additionally, when we perturbed the mitochondrial respiratory chain or the mitochondrial Krebs cycle in CTLs, we did not observe defects in the cortical cytoskeleton during infection (Figures S3C and S3D). These data suggest that the cortical cytoskeleton defects observed in *Pex1* cells are the result of altered peroxisomal metabolism.

Elevated amounts of PA in the cell membrane alter the localization of Rho GTPase and prevent its activation in S2 cells

The Rho family of small GTPases plays a pivotal role in translating extracellular cues, including the signaling arising from microbial detection, into relevant cell responses (Burkhardt, 2013; Yeung et al., 2008). Rac1 and Rho1 (RhoA in mammals) function together to regulate actin cytoskeleton remodeling required for immune cell migration, granule release, formation of immunological synapses, and phagocytosis (Aflaki et al., 2011; Bros et al., 2019; Flannagan et al., 2012; Vicente-Manzanares and Sanchez-Madrid, 2004; Williams, 2007; Zettervall et al., 2004). Distinct GLs at the cell membrane recruit and activate Rho and other signaling proteins. Given that peroxisomes contribute to the GL milieu and defects in the cytoskeleton are evident in *Pex5*-i cells during infection, we asked if peroxisome function was required for the membrane localization of GTPases during microbial challenge.

Rac1 was largely cytoplasmic while Rho1 localized at sites of membrane protrusion in infected CTLs, but both Rac1 and Rho1 appeared as cytoplasmic puncta in *Pex1* cells (Figures 4A–4D). To test if this change in GTPase location in *Pex1* cells also affected the activity of Rac1 and Rho1, we measured the activity of Rac1 and Rho1 in resting and infected CTLs and *Pex1* cells using an ELISA-based assay. Our measurements revealed that both Rac1 and Rho1 are activated in CTLs 30 min after infection but failed to be activated in infected *Pex1* cells (Figures 4E and 4F).

Infected CTLs showed a substantially remodeled cortical actin cytoskeleton, while infected *Pex1* cells showed cortical cytoskeleton and cell protrusion defects (Figures 4G and 4H). We expressed constitutively active forms of either Rac1 (*Rac1V12*) or Rho1 (*Rho1V14*) in CTLs and *Pex1* cells and stained the actin cytoskeleton (Luo et al., 1994). In CTLs, *Rac1V12* induced actin cytoskeleton remodeling and the formation of membrane protrusions in both the presence and absence of *E. coli* (Figures 4G and 4H). *Rac1V12* expression could not rescue the actin cytoskeletal defects of uninfected and infected *Pex1* cells (Figures 4G and 4H), while *Rho1V14* rescued the defects in actin cytoskeleton organization and formation of membrane protrusions in *Pex1* cells (Figures 4G and 4H). The cytoskeleton remodeling that occurs in response to microbial stimuli was dependent on Rho1 activity, as CTLs expressing a dominant negative form of Rho1, *Rho1N19*, failed to form membrane protrusions when infected (Figures 4G and 4H).

Macrophage activation in response to bacterial infection stimulates the cytoskeletal reorganization required for phagosome formation (Mao and Finnemann, 2015). *Pex1* cells or CTLs expressing *Rho1N19* showed reduced uptake of fluorescently labeled *E. coli* compared with CTLs (Figure S4B). This reduction in bacterial uptake by *Pex1* cells was rescued by expression of *Rho1V14* (Figures S4A–S4E).

Plasmatocytes from control adult flies (*Hml > GFP*) showed substantial cortical cytoskeleton staining in response to *E. coli* compared with the round plasmatocytes from *Hml > Pex5*-i flies or *Hml > Rho1N19* flies (Figure 5A). Expression of *Rho1V14* in *Hml > Pex5*-i plasmatocytes (*Hml > Rho1V14;Pex5*-i) rescued cortical cytoskeleton staining in infected cells (Figure 5A). Moreover, like *Hml > Pex5*-i plasmatocytes, infected *Hml > CdsA*-i plasmatocytes remained round and did not develop membrane protrusions (Figure 5A). Expression of *Rho1V14* in *Hml > CdsA*-i plasmatocytes (*Rho1V14*; *Hml > CdsA*-i) rescued cytoskeleton remodeling upon infection (Figure 5A), supporting the concept that metabolic defects caused by PA accumulation in peroxisome-depleted immune cells affect Rho1 signaling needed to trigger cortical cytoskeleton remodeling upon infection. Additionally, flies overexpressing FOXO in plasmatocytes (*Hml > FOXO*) showed the same cytoskeletal defects as *Hml > Pex5*-i and *Hml > CdsA*-i plasmatocytes, but the defects in *Hml > FOXO* plasmatocytes could be rescued by expression of *Rho1V14* (Figure 5A). Ratiometric analysis of cytoplasmic GFP and cortical phalloidin fluorescence indicated that expression of *Rho1V14* in *Hml > Pex5*-i, *Hml > CdsA-i*, and *Hml > FOXO* plasmatocytes rescued their cortical cytoskeleton defects (Figure 5B).

A downstream effector of Rho1 in *Drosophila* and mammals is Rho kinase, which is termed Rok1 or Rock1. Rock1 promotes the recruitment of actin nucleating factors and remodelers such as Diaphanous and myosin II (Khoo et al., 2013) and is involved in regulating immune cell responses to pathogens (Ricker et al., 2016). OE of *Rock1* in *Pex1* cells triggered actin remodeling during infection to yield a cytoskeletal pattern similar to that seen in CTLs (Figures S4F and S4G), confirming that peroxisomes regulate Rho1 signaling to activate cytoskeleton remodeling.

Rho1 signaling in peroxisome-depleted S2 cells is inhibited by p190RhoGAP

PA modulates the activity of Rho GTPases via their regulators, Rho guanine nucleotide exchange factors (RhoGEFs), and Rho GTPase-activating proteins (RhoGAPs) (Ali et al., 2013; Ishihara et al., 2020; Kurooka et al., 2011). RhoGAPs function as effectors or activators of Rho GTPases in response to external stress

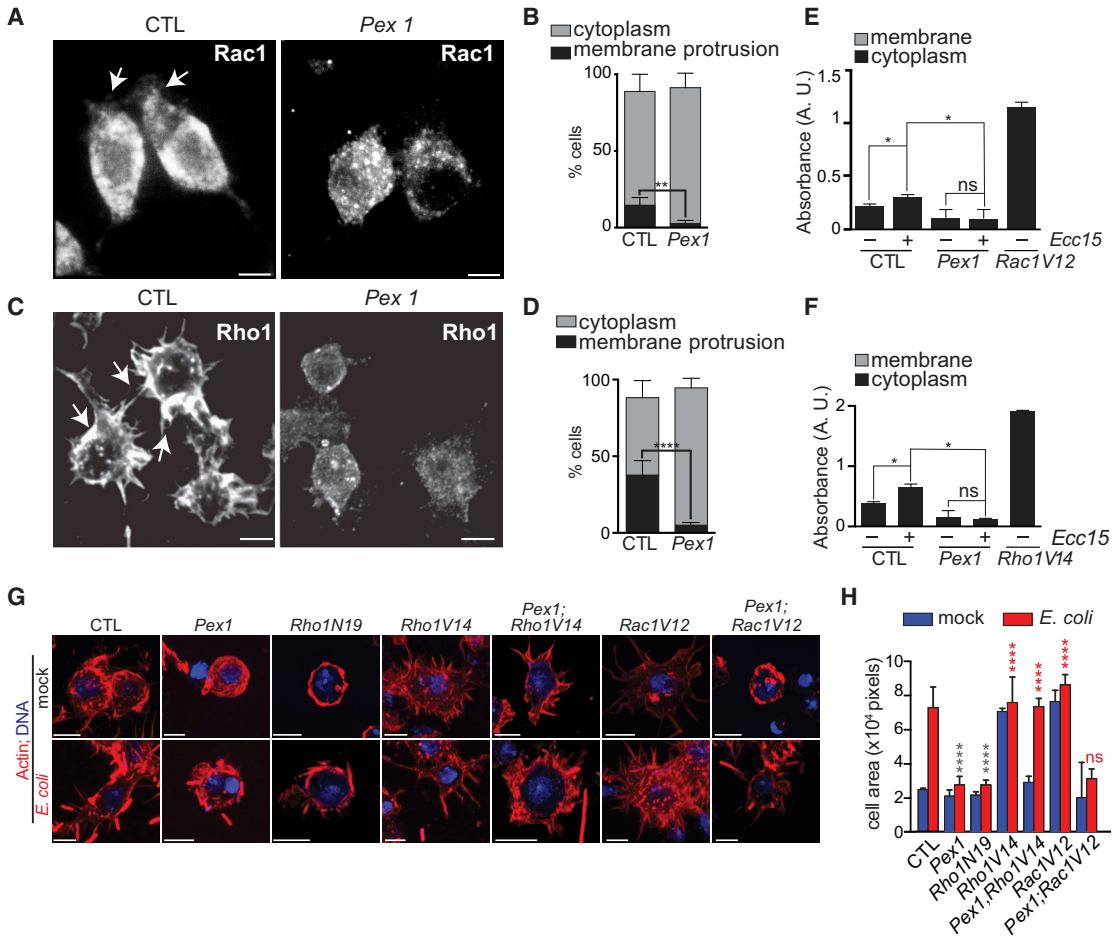

Figure 4. Peroxisomes regulate Rho1-mediated cytoskeleton remodeling in response to bacterial infection

(A) IF microscopy of Rac1. Bar, 10 μm.

(B) Histogram reporting the percentage of cells with Rac1 at membrane protrusions or in the cytoplasm. Values reported are for 30 cells of each genotype.

(C) IF microscopy of Rho1. Bar, 10 μm.

(D) Histogram reporting the percentage of cells with Rho1 at membrane protrusions or in the cytoplasm. Values reported are for 30 cells of each genotype.

(E) Rac1-GTP levels at the membrane or in the cytoplasm in uninfected cells or cells infected with *Ecc15*. 3×10^6 cells of each genotype and under each condition were measured. A.U., arbitrary units.

(F) Rho1-GTPase amounts at the membrane or in the cytoplasm in uninfected cells or cells infected with *Ecc15*. A.U., arbitrary units.

(G) Actin staining in cells of the indicated genotypes. Red rods, *E. coli*; red, actin; blue, DNA. Bar, 10 μm.

(H) Histogram reporting the areas of cells of the indicated genotypes and under the indicated conditions. Values for 30 cells. Values in (B)–(H) are the means ± SD of three independent experiments. Significance was determined by a one-way ANOVA test or by a two-way ANOVA test in (H). ****$p < 0.0001$; **$p < 0.01$; *$p < 0.05$; ns, not significant. Gray asterisks, significance compared with CTLs. Red asterisks, significance compared with *Pex1* cells. See also Figures S2 and S3.

(Bernards and Settleman, 2004). The expression of five genes coding for RhoGAPs was highly upregulated during bacterial infection of *Pex5*-i cells but not CTLs. We performed a mini-RNA interference-based screen to select for RhoGAPs required for cortical cytoskeleton organization and membrane protrusions in S2 cells during infection (Figures S5A and S5B). S2 cells depleted for *RhoGAP5A*, *RhoGAP92B*, or *RhoGAPp190*, but not for *RhoGAP16F* or *RhoGAP54D*, showed alterations in their cortical cytoskeleton when infected compared with when uninfected. Genetic interaction analysis between *Pex1* and each of these *RhoGAP* genes showed that depletion of *RhoGAPp190* rescued the cortical cytoskeleton defects in infected *Pex1* cells (Figures 5C and 5D). In contrast, OE of *RhoGAPp190* in infected CTLs showed cytoskeleton remodeling defects (Figures 5C and 5D). Moreover, *RhoGAPp190* is expressed at higher level in infected *Pex1* cells than in infected CTLs (Figure S5C). CTLs and *Pex1* cells expressing PABD-RFP and a RhoGAPp190-GFP showed colocalization of RhoGAPp190-GFP with PABD-RFP at the membrane in *Pex1* cells (Figures 5E and 5F). However, neither PABD-RFP nor RhoGAP190-GFP was at the plasma membrane in *Pex1* cells when DGK, the enzyme that synthesizes PA from DAG, was depleted (Figures 5E and 5F). Together, these data suggest that in infected *Pex1* cells, RhoGAPp190 is recruited by, or acts in concert with, PA at the cell membrane to inhibit Rho1 signaling and cytoskeleton remodeling, thereby affecting cellular immune responses.

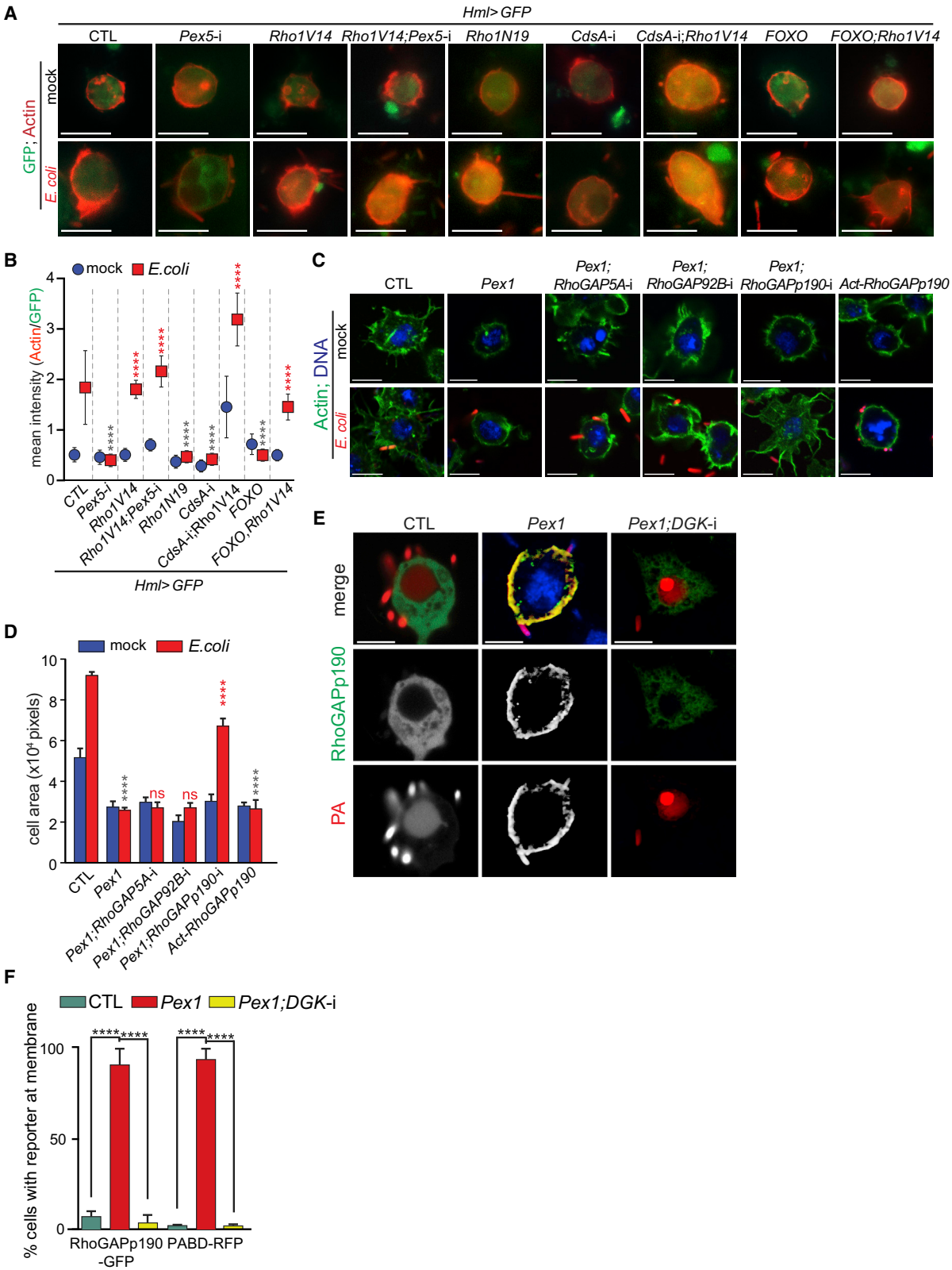

(legend on next page)

Peroxisome-dependent defects in Rho1 signaling decrease host survival of systemic infection

To determine a role for the plasmatocyte peroxisome-GTPase axis in host defense, we assessed the survival of control *Hml > UAS-GFP* (*Hml*) flies with WT plasmatocytes or *Hml > Pex5*-i flies with peroxisome-depleted plasmatocytes expressing different Rho variants after needlestick infection with the entomopathogenic bacterium *Pseudomonas entomophila* (*P.e.*) (Ragheb et al., 2017). We used *P.e.* because it is more pathogenic to *Drosophila* than *Ecc15*, which facilitates the analysis of a requirement for peroxisome-GTPase signaling in host defense under a greater infectious challenge. Uninfected *Hml > Pex5*-i, *Hml > Rho1N19*, *Hml > Rho1V14*, and *Hml > Pex5*-i;*Rho1V14* flies were equally viable as uninfected control *Hml* flies (Figure S5D). Four days after *P.e.* infection, *Hml > Pex5*-i flies showed 40% survival, and *Hml > Rho1N19* flies showed 60% survival (Figure S5D). Infected *Hml > Pex5*-i and *Hml > Rho1N19* flies died at a faster rate than *Hml* control flies (Figure S5D). *Rho1V14* expression in *Hml > Pex5*-i flies (*Hml > Pex5*-i;*Rho1V14)* rescued survival to levels observed in control *Hml* flies and similar to survival levels observed for *Hml > Rho1V14* flies, with 40% of flies surviving 8 days post-infection.

Hml > Pex5-i flies and *Hml > Rho1N19* flies showed higher pathogen load than *Hml > Rho1V14* flies and *Hml > Pex5*-i;*Rho1V14* flies infected with *P.e* (Figure S5E). Thus, depletion of *Pex5* or expression of *Rho1N19* in plasmatocytes made flies more susceptible to infection.

Peroxisomes promote Rho1-mediated cytokine secretion by plasmatocytes in *Drosophila*

Septic injury in *Drosophila* induces the secretion of the cytokine Unpaired3 (Upd3), which is orthologous to mammalian interleukin-6 (Agaisse et al., 2003), by plasmatocytes (Agaisse and Perrimon, 2004; Pean et al., 2017; Yang et al., 2015). Cytokine secretion relies on Rho GTPases during vesicle trafficking, a process that is broadly conserved among cytokine-producing cells (Fessler et al., 2007). To determine the effects of peroxisome-mediated Rho signaling and cytoskeleton remodeling on cytokine secretion, we tested the ability of plasmatocytes from *Hml > Pex5*-i flies to secrete Upd3 in response to infection. Upd3 secretion was followed using an Upd3-GFP reporter. Upd3-GFP was not observed in the body cavity of uninfected control *Hml > Upd3-GFP* flies or uninfected *Hml > Pex5*-i;*Upd3-GFP* flies (Figure 6A, panels at left). 73% of control *Hml > Upd3-GFP* flies infected with *Ecc15* showed GFP in the body cavity within 6 h of infection, while no infected *Hml > Pex5*-i;*Upd3-GFP* flies showed GFP in the body cavity (Figure 6A, panels at right). However, GFP was observed in the body cavity in 64% of infected flies when *Rho1V14* was expressed in *Hml > Pex5*-i flies (*Hml > Pex5*-i;*Rho1V14)*. Intriguingly, *Hml > CdsA*-i flies, which are depleted for the enzyme that converts PA to CDP-DAG and thus accumulate PA (Figure 2B), did not show *Upd3-GFP* in the body cavity when infected (Figure 6A, panels at right). Our data show that peroxisomes regulate the secretion of the immune-responsive cytokine Upd3 in response to bacterial infection by contributing to the cellular glycerophospholipid milieu required to activate Rho1-mediated cytoskeleton remodeling and to initiate the immune response.

Peroxisomal metabolism regulates Rho1-mediated cytokine secretion by murine macrophages

We analyzed bone marrow-derived macrophages (BMDMs) from homozygous *Peroxin2* (*Pex2*$^{-/-}$) mutant mice to assess whether peroxisomal metabolic control of GL amounts promotes cytoskeleton remodeling and activation of mammalian macrophages as measured by cytokine release. The *Pex2* gene encodes a ubiquitin ligase (Biermanns et al., 2003) needed to recycle the *Pex5* receptor (Smith and Aitchison, 2013). *Pex2*$^{-/-}$ mice carry a recessive mutation in both copies of the *Pex2* gene (Figures S6A and S6B) and show peroxisome biogenesis defects similar to those observed in *Pex5* mutant mice, such as a loss of targeting of catalase to peroxisomes (Figure S6C). Because *Pex5*$^{-/-}$ mice die at birth, we chose to use *Pex2*$^{-/-}$ mice for our studies, as they can survive up to 20 days.

We previously reported a requirement of peroxisomes for phagocytosis (Di Cara et al., 2017). We therefore tested the ability of *Pex2*$^{-/-}$ BMDMs to engulf fluorescently labeled bacteria. *Pex2*$^{-/-}$ BMDMs engulfed 30%–40% less bacteria than BMDMs from littermate control mice (Figure S6D). Compromised phagocytosis in *Pex2*$^{-/-}$ BMDMs was not associated with defects in macrophage development, as *Pex2*$^{-/-}$ macrophage maturation was intact (Figures S6E and S6F). These results suggest that Pex2 is required for peroxisomes to drive phagocytosis.

We assayed the cytokine response in *Pex2*$^{-/-}$ BMDMs to test if Pex2 is required for cytokine release in response to immune elicitors, as has been observed for *Pex5* in *Drosophila*. Using a cytokine array, we screened for a variety of cytokines and chemokines released by *Pex2*$^{-/-}$ BMDMs after stimulation with LPS. *Pex2*$^{-/-}$ BMDMs secreted few cytokines and chemokines in response to LPS stimulation compared with WT BMDMs (Figures 6B and 6C). We confirmed that LPS-treated *Pex2*$^{-/-}$ BMDMs did not secrete detectable IL-6 and TNF-α, and they

Figure 5. Peroxisomal metabolism mediates signaling by RhoGAPp190-Rho1

(A) Detection of actin and membrane protrusions in plasmatocytes of the indicated genotypes. Green, cytoplasmic GFP; red rods, *E. coli*; red, actin. Bar, 10 μm.

(B) Histogram reporting the ratios of phalloidin fluorescence intensity to GFP fluorescence intensity in plasmatocytes of the indicated genotypes and under the indicated conditions. Gray asterisks, significance compared with control *Hml > GFP* plasmatocytes. Red asterisks, significance compared with *Hml > GFP*; *Pex5*-i plasmatocytes.

(C) Detection of actin and membrane protrusions in cells of the indicated genotypes. Green, actin; red rods, *E. coli*; blue, DNA. Bar, 10 μm.

(D) Histogram reporting areas of cells of the indicated genotypes and under the indicated conditions. Gray asterisks, significance compared with CTLs. Red asterisks, significance compared with *Pex1* cells.

(E) Imaging of the PA reporter, PABD-RFP, and of RhoGAPp190-GFP. Bar, 10 μm.

(F) Histogram reporting the percentage of cells with RhoGAPp190-GFP or PABD-RFP at the membrane in cells of the indicated genotype. Values in (B), (D), and (F) are the means ± SD of three independent experiments totaling 30 cells. Significance was determined using a one-way ANOVA test in (B), a two-way ANOVA test in (D), and Student's *t* test. ****p < 0.0001. See also Figures S4 and S5.

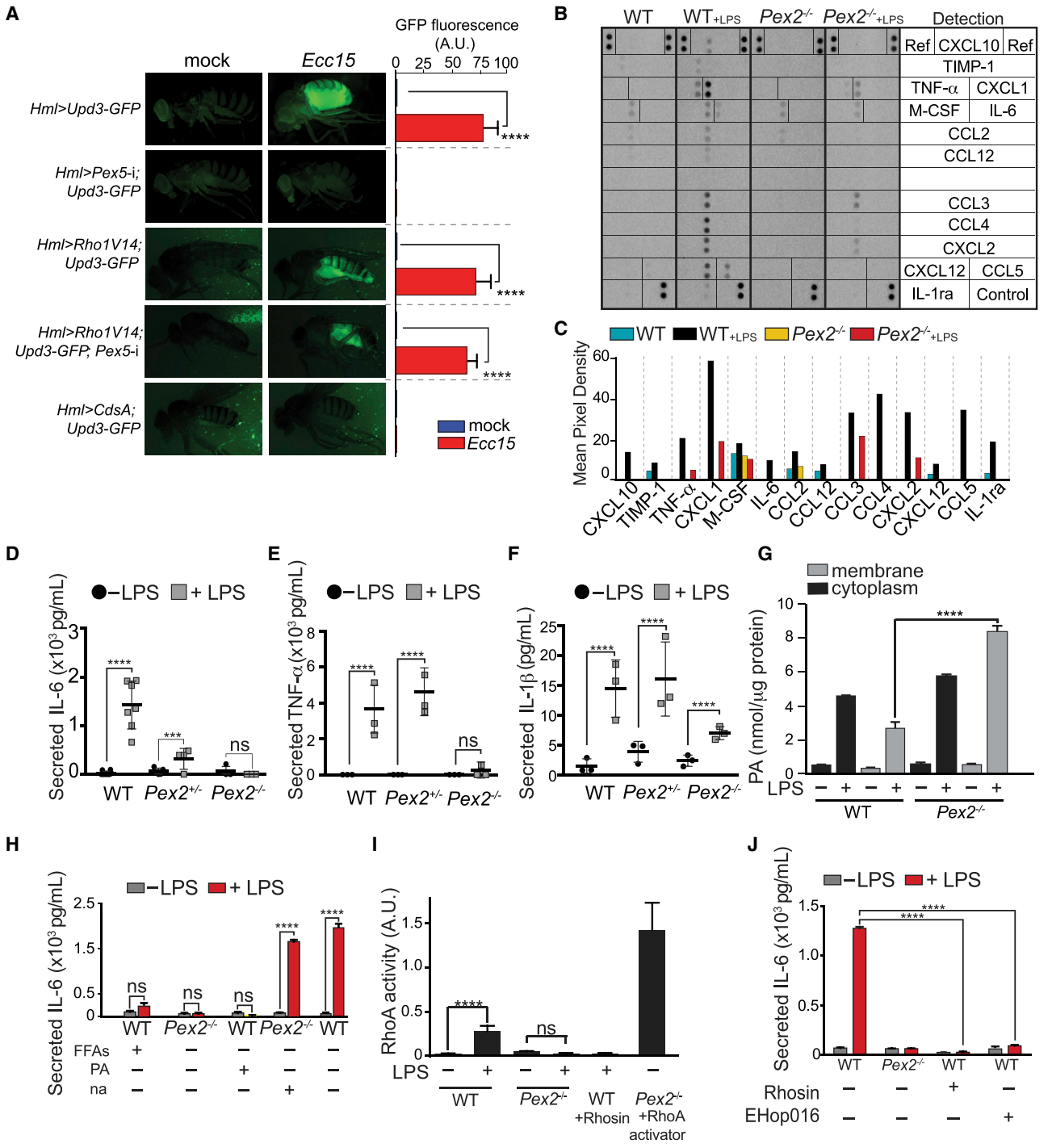

Figure 6. Peroxisome metabolism regulates Rho1-mediated cytokine release in response to microbial challenge in *Drosophila* and mouse

(A) Thoracic injection of bacteria into adult flies triggers secretion of the cytokine Upd3 by plasmatocytes.

(B) Mouse cytokine array analysis of cytokines and chemokines secreted by WT and *Pex2*$^{-/-}$ BMDMs in the absence or presence of LPS.

(C) Histogram reporting the mean pixel density for each spot detected in the mouse cytokine array for BMDMs of the two genotypes and under the two conditions.

(D–F) IL-6 (D), TNF-α (E), and IL-1β (F) secretion by WT, *Pex2*$^{+/-}$, and *Pex2*$^{-/-}$ BMDMs in the absence or presence of LPS.

(G) Histogram reporting the amount of PA in membrane and cytoplasmic fractions isolated from WT and *Pex2*$^{-/-}$ BMDMs that were unstimulated or stimulated with LPS.

(H) Histogram reporting the amount of IL-6 secreted by WT and *Pex2*$^{-/-}$ BMDMs under the indicated treatments.

(legend continued on next page)

secreted very low levels of IL-1β compared with the levels secreted by WT or *Pex2* heterozygous (*Pex2*$^{+/-}$) BMDMs (Figures 6D–6F). However, measurement of transcripts for IL-6, TNF-α, and IL-1β by qRT-PCR revealed that *Pex2*$^{-/-}$ BMDMs had the same transcript levels for these cytokines as did WT and *Pex2*$^{+/-}$ BMDMs (Figure S6G). Because of this observation, we assessed IL-6 and TNF-α protein synthesis in *Pex2*$^{-/-}$ BMDMs and saw granules containing IL-6 and TNF-α in LPS-treated *Pex2*$^{-/-}$ BMDMs (Figures S6H and S6I). Together, these data show that Pex2 is needed for cytokine release by macrophages but not for cytokine gene transcription or mRNA translation.

Given the lipid metabolic defects we observed in *Drosophila Pex5*-i and *Pex1* macrophages and their effects on cytoskeleton remodeling and Upd3 cytokine release, we tested whether similar lipid metabolic defects were linked to cytokine secretion by *Pex2*$^{-/-}$ BMDMs. We measured PA in LPS-treated WT and *Pex2*$^{-/-}$ BMDMs and found greater amounts of PA in the membrane fraction and lesser amounts in the cytoplasm fraction of *Pex2*$^{-/-}$ BMDMs compared with WT BMDMs (Figure 6G). Like *Pex1* fly macrophages, LPS-treated *Pex2*$^{-/-}$ BMDMs had lower amounts of PIP3 in their membranes (Figure S6J). Moreover, PIP2 was detected in LPS-treated WT BMDMs but not in LPS-treated *Pex2*$^{-/-}$ BMDMs (Figure S6K). Thus, *Pex2*$^{-/-}$ murine macrophages exhibit similar alterations in their GL profiles to those observed in *Drosophila* S2 cells.

We next tested whether the altered cellular lipid environment observed in peroxisome-depleted *Pex2*$^{-/-}$ BMDMs was linked to changes in cytokine secretion by these cells. When WT BMDMs were treated with an FFA cocktail or PA, LPS-induced IL-6 secretion was inhibited (Figure 6H). Moreover, *Pex2*$^{-/-}$ BMDMs treated with niacin, an FFA scavenger, were able to secrete IL-6 upon LPS stimulation (Figure 6H).

To evaluate whether mutation of *Pex2*, together with the associated GL metabolic defects in murine macrophages, affected Rho-dependent cytoskeleton remodeling and cytokine secretion as seen in *Drosophila*, we measured the activity of RhoA, the orthologue of *Drosophila* Rho1, in LPS-treated WT and *Pex2*$^{-/-}$ BMDMs. RhoA activity increased in WT BMDMs 20 min after LPS addition, while it remained unchanged in *Pex2*$^{-/-}$ BMDMs and WT BMDMs treated with the RhoA inhibitor, Rhosin (Figure 6I). However, *Pex2*$^{-/-}$ BMDMs treated with a RhoA activator, CN04, showed greatly increased RhoA activity. WT BMDMs treated with Rhosin or the broad spectrum GTPase inhibitor, EHop016, did not secrete IL-6 upon LPS treatment (Figure 6J), suggesting that RhoA signaling is needed for IL-6 secretion by mouse macrophages.

We next assessed if defects in the cellular lipid milieu, RhoA signaling, and cytokine secretion were due to disruption of the macrophage cortical actin organization. Infected *Pex2*$^{-/-}$ BMDMs lacked membrane protrusions and exhibited a less organized cortical cytoskeleton, as measured by a smaller mean cell area, than that of infected WT BMDMs (Figures 7A and 7B). The cortical cytoskeleton of WT BMDMs treated with PA or with a cocktail of FFAs was less organized than that of untreated WT BMDMs (Figures 7A and 7B). In contrast, *Pex2*$^{-/-}$ BMDMs treated with niacin showed a cortical cytoskeleton organization like that of WT BMDMs (Figures 7A and 7B), confirming that the lipid defects present in *Pex2*$^{-/-}$ BMDMs inhibit cytoskeleton remodeling. In addition, WT BMDMs treated with Rhosin showed cortical cytoskeleton defects (Figures 7A and 7B). Of note, treatment of *Pex2*$^{-/-}$ BMDMs with a RhoA activator rescued the cytoskeleton defects seen in untreated cells (Figures 7A and 7B). Together these data suggest that mutation in the peroxisome biogenesis factor *Pex2* causes changes in the GL milieu that are linked to Rho-GTPase-mediated cortical actin remodeling and cytokine release in challenged BMDMs.

Since LPS is a Toll-like receptor (TLR) 4 agonist, we next investigated whether peroxisomal metabolism affects only TLR4-dependent cytokine responses or also cytokine responses dependent on other TLRs. We stimulated WT and *Pex2*$^{-/-}$ BMDMs with Pam3CSK4, a TLR1 and TLR2 agonist, and with R848, a TLR7 and TLR8 agonist (Geng et al., 2015). *Pex2*$^{-/-}$ BMDMs did not secrete IL-6 in response to treatment with Pam3CSK4 but did secrete IL-6 in response to treatment with R848 (Figures S6L and S6M). Because TLR1, TLR2, and TLR4 are located at the cell membrane, and TLR7 and TLR8 are intracellular, the different responses of *Pex2*$^{-/-}$ BMDMs to Pam3CSK4 and R848 suggest that *Pex2*$^{-/-}$ mutation may affect signaling arising at the cell surface but not intracellularly. Together, our data support a scenario in which peroxisomes direct cellular lipid metabolism, contribute to GL production and localization, and promote cytoskeleton rearrangement, all of which combine to allow the cell to translate signals from outside the cell to inside the cell to control immune defense mechanisms such as proinflammatory cytokine release.

Peroxisomal lipid metabolism is needed for proinflammatory responses from human peripheral blood mononuclear cells

Rho GTPases and their downstream effector kinases control immune cell mobilization and secretion of proinflammatory cytokines in response to stimuli. Dysregulation of these signaling cascades contributes to proinflammatory immune disorders characterized by aberrant cytokine production and unresolved inflammation resulting from unwarranted immune responses (Biro et al., 2014). Given the conserved role that peroxisomes play in the regulation of cytoskeleton-mediated immune processes, including activation of proinflammatory responses in macrophages, we investigated whether peroxisomes are associated with chronic inflammatory phenotypes. We examined peripheral blood mononuclear cells (PBMCs) of patients affected by the severe inflammatory disorder Kawasaki disease (KD). PBMCs from KD patients had more anti-SKL-positive staining of peroxisomes than PBMCs from healthy donors (Figures 7C and 7D). PBMCs from KD patients had reduced amounts of PA

(I) Histogram reporting RhoA GTPase activity in WT and *Pex2*$^{-/-}$ BMDMs under the reported treatments.
(J) Histogram reporting the amount of IL-6 secreted by WT and *Pex2*$^{-/-}$ BMDMs under the reported treatments. Values reported are means ± SD of three independent experiments in (A) and (E)–(J), and of six independent experiments in (D). Statistical significance in (A) and (D)–(J) was determined using Student's *t* test. ****$p < 0.0001$; ***$p < 0.001$; ns, not significant. See also Figure S6.

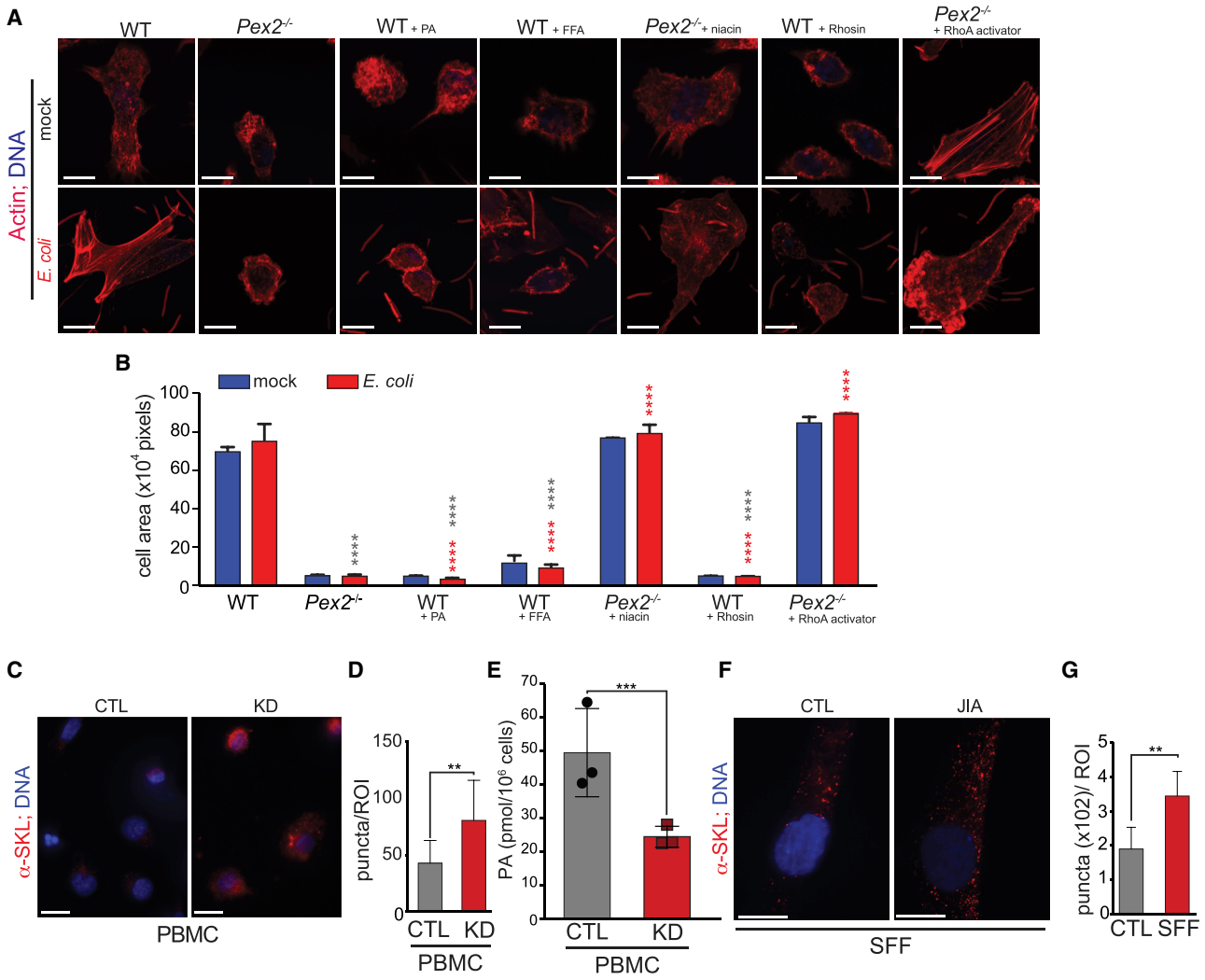

Figure 7. Peroxisomal metabolism contributes to inflammatory responses

(A) Actin staining in WT and *Pex2*$^{-/-}$ BMDMs under the indicated conditions. Red, actin; red rods, *E. coli*; blue, DNA. Bar, 10 μm.

(B) Histogram reporting the areas of BMDMs of the indicated genotypes and under the indicated conditions. Gray asterisks, significance compared with WT BMDMs; red asterisks, significance compared with *Pex2*$^{-/-}$ BMDMs.

(C) IF microscopy of anti-SKL antibody (α-SKL) staining in PBMCs from healthy individuals (CTL) or KD patients. Red, α-SKL; blue, DNA. Bar, 10 μm.

(D) Histogram reporting the number of α-SKL-positive puncta per region of interest (ROI) in CTL or KD PBMCs.

(E) Histogram reporting PA amounts in the cell membrane fraction from LPS-treated CTL and KD PBMCs.

(F) IF microscopy of α-SKL staining of SFFs from healthy individuals (CTL) and JIA patients. Red, α-SKL; blue, DNA. Bar, 10 μm.

(G) Histogram reporting the number of α-SKL-positive puncta per ROI in CTL or JIA SFFs. Values are means ± SD of four independent experiments totaling 20 cells in B, of two independent experiments totaling 30 ROIs in (D) and (G), and of three independent experiments in (E). Significance in (B), (D), (E), and (G) was determined using Student's *t* test. ****p < 0.0001; ***p < 0.001; **p < 0.01. See also Figures S6 and S7.

compared with control PBMCs (Figure 7E), suggesting that immune cells with increased numbers of peroxisomes have reduced amounts of PA and exhibit a severe inflammatory phenotype.

We next treated healthy donor PBMCs with LPS or a cocktail of proinflammatory cytokines (IL-6, IL-1β, TNF-α) to reproduce the inflammatory properties of KD PBMCs. FC analysis showed that healthy donor PBMCs treated for 24 h with LPS exhibited more anti-SKL-positive staining than untreated healthy donor PBMCs (Figures S7A and S7D). The increase in anti-SKL-positive staining was observed specifically in B cells (CD19+) and monocytes (CD14+) (Figures S7A and S7D) but not in NK cells (CD56+) or T cells (CD8+, CD4+) (Figures S7B, S7C, and S7E). Similar results were obtained with the cytokine cocktail (Figure S7).

We next analyzed synovial fluid fibroblasts (SFFs) from juvenile idiopathic arthritis (JIA) patients for further evidence that peroxisomes support a cellular inflammatory phenotype. SFFs from JIA patients exhibit a strong inflammatory phenotype and are considered the primary source of the proinflammatory cytokine

storm that drives joint inflammation in JIA patients. Fibroblasts from JIA patients exhibited increased numbers of anti-SKL positive puncta than SFFs from healthy individuals (Figures 7F and 7G). Thus, cells exhibiting an inflammatory phenotype had more peroxisomes and reduced amounts of PA in their cell membrane than cells not exhibiting an inflammatory phenotype. These data in human cells are in our agreement with our results from *Drosophila* and mouse macrophages showing low inflammation and high amounts of PA in cells lacking functional peroxisomes.

DISCUSSION

Evidence showing that metabolic programs govern specific immune cell functions has grown (Hooftman et al., 2020; O'Neill et al., 2016; O'Neill and Pearce, 2016; Ryan and O'Neill, 2020). Dysregulation of lipid metabolism has been implicated in the aberrant function of macrophages in diseases such as atherosclerosis and obesity and in certain intracellular infections (Yan and Horng, 2020). Here, we explored the contribution of the peroxisome, a key metabolic organelle, to the lipid-mediated signaling that guides the macrophage response to acute infection. Using *Drosophila*, a well-known model system for studying immune and metabolic signaling (Galenza and Foley, 2019; Lemaitre and Hoffmann, 2007), we found that peroxisomal metabolism contributes to the GL milieu required to mediate processes of macrophage immune activation, such as cytokine release.

Actin remodeling enables the reorganization of the plasma membrane needed for proper receptor localization, recruitment of signaling intermediates, and changes in cell morphology required for macrophage immune activation. Thus, actin remodeling regulates many of the cellular programs that drive macrophage differentiation, activation, proliferation, and survival. We have shown that peroxisomes are pivotal to triggering actin remodeling cascades in macrophages during the early stages of infection. The importance of regulating the actin cytoskeleton for leukocyte function is emphasized by conditions such as neutropenia and by animal models of immunodeficiency in which genes involved in regulating actin have been targeted. It is now clear that mutations in cytoskeletal proteins can lead to immunodeficiency or autoimmunity, and that pathogens subvert immune cells by manipulating cytoskeletal dynamics (Salzer et al., 2020).

Rho GTPases are known regulators of actin dynamics and rearrangement (Mao and Finnemann, 2015). Rho GTPases contribute to immune cell function, and serious immune dysfunctionalities have been shown to be due to defects in individual GTPases (Arbibe et al., 2000; Bokoch, 2005) and their regulators (Biro et al., 2014). A specific composition of GLs within the plasma membrane is required to activate key cytoskeletal remodeling factors such as Rho1 in *Drosophila* cells and RhoA in mammalian cells (Aflaki et al., 2011; Bros et al., 2019; Flannagan et al., 2012; Sit and Manser, 2011; Williams, 2007; Zettervall et al., 2004). Our findings in both fly and mouse show that peroxisomal β-oxidation contributes to changes in plasma membrane GL composition that control cytoskeleton remodeling that in turn contributes to the macrophage's capacity to mount an immune response to microbial challenge by modulation of the Rho1/RhoA cascade. Specifically, we observed that a high concentration of PA accumulates in the plasma membrane of *Pex1* cells. The amounts of PA in the cell change dynamically in response to external stimuli, and PA is important for mediating diverse cellular and physiological processes in eukaryotes. For example, PA plays a central role in the recruitment of proteins to the plasma membrane to promote signal transduction, and PA can modulate the activity of the Rho family of GTPases and their regulators, RhoGEFs and RhoGAPs (Ali et al., 2013; Ishihara et al., 2020; Kurooka et al., 2011). Some studies have concluded that RhoGAPs function as negative regulators of Rho GTPases (Bernards and Settleman, 2004), such that inhibition of RhoGAP activity is sufficient to promote Rho activation and downstream responses. We showed that RhoGAPp190 is regulated by PA, a peroxisome metabolite, which inhibits Rho1 and immune cell activation. Of note, the two RhoGAPp190s in the mammalian genome, p190-A and p190-B, are tightly regulated transcriptionally and post-transcriptionally in response to external changes such as increased insulin levels or exposure to alcohol (Bernards and Settleman, 2004; Heraud et al., 2019), supporting their important role in responding to stressors. Our study adds to our understanding of the complex mechanisms that regulate Rho GTPase signaling and identify a specific role for RhoGAPp190 as a negative regulator of the macrophage response to microbial stimuli.

Our findings have implications for a variety of immune and inflammatory conditions with underlying lipid metabolic defects, such as atherosclerosis, autoimmune disease, and conditions like osteoarthritis that exhibit local or systemic changes in PA (Singh and Aballay, 2017). Our observations that peroxisome numbers increase in response to inflammatory stimuli in both mouse and human cells and that peroxisome numbers were elevated in the PBMCs of KD patients and SFFs of JIA patients suggest that peroxisome-mediated lipid changes impact the inflammatory status of immune cells. Our study paves the way for further studies aimed at defining the immunomodulatory roles of peroxisomes and how lipids that control inflammatory signaling in immune disorders are regulated, potentially opening up therapeutic avenues for treating these disorders. Overall, our findings reveal the peroxisome to be a major modulator of multiple cellular immune functions across diverse phyla.

Limitation of the study

Glycerophospholipids are key signaling molecules in many cell signaling pathways, including those involved in immunity. Glycerophospholipids can be produced by various pathways located in different subcellular compartments. Here, we define the peroxisome, a ubiquitous membrane-enclosed organelle, as an important contributor to glycerophospholipid signaling that regulates immune defense processes in macrophages.

There are limitations to our study. We were unable to define if the signaling lipids, PA and phosphatidylinositol phosphates (PIPs), are made by the peroxisome and if their amounts in the cell are indirectly affected by dysfunction in peroxisomal β-oxidation. Also, the size of S2 cells hampered us in determining whether peroxisomes recruit the enzymes required to produce PA and PIPs. Given that our current study shows this signaling pathway is conserved in mammalian cells, we are confident that murine or human macrophages would be suitable for these future studies.

Finally, we identified PA as a metabolic marker of inflammation in cells of patients affected by autoimmune disease. However, we could not define a mechanism linking peroxisomes, PA accumulation, and inflammatory signaling. Finding this link is an ongoing pursuit for our team.

STAR★METHODS

Detailed methods are provided in the online version of this paper and include the following:

- KEY RESOURCES TABLE
- RESOURCE AVAILABILITY
  - Lead contact
  - Materials availability
  - Data and code availability
- EXPERIMENTAL MODEL AND SUBJECT DETAILS
  - Fly cell culture
  - Fly stocks, husbandry and microinjection
  - Mammalian cells
  - Human peripheral blood mononuclear cells
  - Human synovial fluid fibroblasts
  - Bacteria
  - *Pex2* mutant mice
- METHOD DETAILS
  - Reagents
  - Macrophage treatment with Rho GTPase inhibitors and activator
  - Treatment of murine BMDMs with fatty acids, phosphatidic acid, and niacin
  - Treatment of murine BMDMs with lipopolysaccharides, Pam3CSK4 and R848, and cytokine detection and measurements
  - Constructs
  - Assay for Rho GTPase activation
  - Lipidomics
  - Heatmaps
  - RNA-seq
  - RNA extraction and qRT-PCR
  - Mitochondrial respiration rate
  - Bacterial burden and survival rate of adult flies
  - Isolation of cell membranes
  - Quantification of FFAs, PA and PIP3
  - Immunofluorescence microscopy
  - Live-cell imaging
  - Flow cytometry
  - Multi-spectral imaging flow cytometry (IFC)
  - Internalization assay
- QUANTIFICATION AND STATISTICAL ANALYSIS
  - Statistical analysis
  - Quantification of cell area defined by phalloidin staining
  - Quantification of signaling molecule location
  - Quantification of SKL-labeled puncta

SUPPLEMENTAL INFORMATION

Supplemental information can be found online at https://doi.org/10.1016/j.celrep.2022.110433.

ACKNOWLEDGMENTS

This work was funded by a Project Grant from the Canadian Institutes of Health Research to F.D., a Discovery Grant from the Natural Sciences and Engineering Research Council of Canada to F.D., a Canada Foundation for Innovation JELF equipment grant to F.D., a Dalhousie Medical Research Foundation start-up fund to F.D., an IWK Foundation graduate student scholarship to Y.M., an IWK Foundation summer studentship to I.E., and a GIVETOLIVE sponsored Beatrice Hunter summer studentship to C.M.W.

Flow cytometry was performed at the University of Alberta, Faculty of Medicine & Dentistry Flow Cytometry Facility and at the Dalhousie University, Faculty of Medicine Flow Cytometry Core Facility. Microscopy was performed at the Dalhousie University, Faculty of Medicine Cellular and Molecular Digital Imaging and Zebrafish Core Facility. We thank Stephen Withefield and Brianne Lindsay for help with microscopy, and Aja Rieger and Derek Rowter for training and for technical help in flow cytometry. David Malloy provided access to the Dalhousie Zebrafish Core Fluorescent Stereomicroscopes for *Drosophila* imaging.

Lipidomic analysis was performed at the University of Amsterdam Medical Centers, Laboratory Genetic Metabolic Diseases, Core Facility Metabolomics.

AUTHOR CONTRIBUTIONS

A.S.N., F.D., and B.D.P. performed experiments using *Drosophila* cell lines. S.M. performed IF microscopy of *Rho1*-transfected cells. J.L. and F.D. did the PIP2 analysis. Y.M. characterized the FOXO response to peroxisomal metabolic defects. C.M.W., I.E., and K.A.F. made lipid and Rho1 reporter constructs and performed microscopy of transfected cells. R.L.C., P.M.S., F.D., and B.D.P. performed mouse experiments. P.M.S. performed flow cytometry analysis. D.P.M. performed live-imaging analysis. A.P.M. and Y.H. advised on experiments using mice. L.H.B. and N.P. analyzed mitochondrial activities. B.D. supplied cells from KD and JIA patients. C.W. established the *Pex2* mutant mouse colony. A.J.S. constructed RNA libraries for next generation sequencing analysis. R.A.R. advised on experimental design and contributed to writing the manuscript. F.D. conceived the project, performed experiments and analyses, and wrote the manuscript with B.D.P. and R.A.R.

DECLARATION OF INTERESTS

All authors declare no competing interests.

INCLUSION AND DIVERSITY

We worked to ensure gender balance in the recruitment of human subjects. We worked to ensure ethnic or other types of diversity in the recruitment of human subjects. We worked to ensure that the study questionnaires were prepared in an inclusive way. We worked to ensure sex balance in the selection of non-human subjects. We worked to ensure diversity in experimental samples through the selection of the cell lines. We worked to ensure diversity in experimental samples through the selection of the genomic datasets. One or more of the authors of this paper self-identifies as an underrepresented ethnic minority in science. One or more of the authors of this paper self-identifies as a member of the LGBTQ+ community. One or more of the authors of this paper self-identifies as living with a disability. One or more of the authors of this paper received support from a program designed to increase minority representation in science.

Received: March 22, 2021
Revised: December 21, 2021
Accepted: February 1, 2022
Published: March 1, 2022

REFERENCES

Acharya, U., and Acharya, J.K. (2005). Enzymes of sphingolipid metabolism in *Drosophila melanogaster*. Cell. Mol. Life Sci. *62*, 128–142.

Aderem, A., and Underhill, D.M. (1999). Mechanisms of phagocytosis in macrophages. Annu. Rev. Immunol. *17*, 593–623.

Agaisse, H., and Perrimon, N. (2004). The roles of JAK/STAT signaling in *Drosophila* immune responses. Immunol. Rev. *198*, 72–82.

Aflaki, E., Balenga, N.A., Luschnig-Schratl, P., Wolinski, H., Povoden, S., Chandak, P.G., Bogner-Strauss, J.G., Eder, S., Konya, V., Kohlwein, S.D., et al. (2011). Impaired Rho GTPase activation abrogates cell polarization and migration in macrophages with defective lipolysis. Cell. Mol. Life Sci. *68*, 3933–3947.

Agaisse, H., Petersen, U.M., Boutros, M., Mathey-Prevot, B., and Perrimon, N. (2003). Signaling role of hemocytes in *Drosophila* JAK/STAT-dependent response to septic injury. Dev. Cell *5*, 441–450.

Akasaki, Y., Alvarez-Garcia, O., Saito, M., Carames, B., Iwamoto, Y., and Lotz, M.K. (2014). FoxO transcription factors support oxidative stress resistance in human chondrocytes. Arthritis Rheumatol. *66*, 3349–3358.

Ali, W.H., Chen, Q., Delgiorno, K.E., Su, W., Hall, J.C., Hongu, T., Tian, H., Kanaho, Y., Di Paolo, G., Crawford, H.C., et al. (2013). Deficiencies of the lipid-signaling enzymes phospholipase D1 and D2 alter cytoskeletal organization, macrophage phagocytosis, and cytokine-stimulated neutrophil recruitment. PLoS One *8*, e55325.

Arbibe, L., Mira, J.P., Teusch, N., Kline, L., Guha, M., Mackman, N., Godowski, P.J., Ulevitch, R.J., and Knaus, U.G. (2000). Toll-like receptor 2-mediated NF-κB activation requires a Rac1-dependent pathway. Nat. Immunol. *1*, 533–540.

Basset, A., Khush, R.S., Braun, A., Gardan, L., Boccard, F., Hoffmann, J.A., and Lemaitre, B. (2000). The phytopathogenic bacteria *Erwinia carotovora* infects *Drosophila* and activates an immune response. Proc. Natl. Acad. Sci. U S A *97*, 3376–3381.

Bassett, A.R., Tibbit, C., Ponting, C.P., and Liu, J.L. (2014). Mutagenesis and homologous recombination in *Drosophila* cell lines using CRISPR/Cas9. Biol. Open *3*, 42–49.

Battiprolu, P.K., Hojayev, B., Jiang, N., Wang, Z.V., Luo, X., Iglewski, M., Shelton, J.M., Gerard, R.D., Rothermel, B.A., Gillette, T.G., et al. (2012). Metabolic stress-induced activation of FoxO1 triggers diabetic cardiomyopathy in mice. J. Clin. Invest. *122*, 1109–1118.

Becker, T., Loch, G., Beyer, M., Zinke, I., Aschenbrenner, A.C., Carrera, P., Inhester, T., Schultze, J.L., and Hoch, M. (2010). FOXO-dependent regulation of innate immune homeostasis. Nature *463*, 369–373.

Bernards, A., and Settleman, J. (2004). GAP control: regulating the regulators of small GTPases. Trends Cell Biol. *14*, 377–385.

Biermanns, M., von Laar, J., Brosius, U., and Gartner, J. (2003). The peroxisomal membrane targeting elements of human *peroxin 2* (*PEX2*). Eur. J. Cell Biol. *82*, 155–162.

Biro, M., Munoz, M.A., and Weninger, W. (2014). Targeting Rho-GTPases in immune cell migration and inflammation. Br. J. Pharmacol. *171*, 5491–5506.

Bokoch, G.M. (2005). Regulation of innate immunity by Rho GTPases. Trends Cell Biol. *15*, 163–171.

Bros, M., Haas, K., Moll, L., and Grabbe, S. (2019). RhoA as a key regulator of innate and adaptive immunity. Cells *8*, 733.

Burkhardt, J.K. (2013). Cytoskeletal function in the immune system. Immunol. Rev. *256*, 5–9.

Cabrera-Ortega, A.A., Feinberg, D., Liang, Y., Rossa, C., Jr., and Graves, D.T. (2017). The role of Forkhead box 1 (FOXO1) in the immune system: dendritic cells, T cells, B cells, and hematopoietic stem cells. Crit. Rev. Immunol. *37*, 1–13.

Cherry, S. (2008). Genomic RNAi screening in *Drosophila* S2 cells: what have we learned about host-pathogen interactions? Curr. Opin. Microbiol. *11*, 262–270.

Cliff, J.M., King, E.C., Lee, J.S., Sepulveda, N., Wolf, A.S., Kingdon, C., Bowman, E., Dockrell, H.M., Nacul, L., Lacerda, E., et al. (2019). Cellular immune function in myalgic encephalomyelitis/chronic fatigue syndrome (ME/CFS). Front. Immunol. *10*, 796.

Dasgupta, U., Bamba, T., Chiantia, S., Karim, P., Tayoun, A.N.A., Yonamine, I., Rawat, S.S., Rao, R.P., Nagashima, K., Fukusaki, E., et al. (2009). Ceramide kinase regulates phospholipase C and phosphatidylinositol 4, 5, bisphosphate in phototransduction. Proc. Natl. Acad. Sci. U S A *106*, 20063–20068.

Deane, J.A., and Fruman, D.A. (2004). Phosphoinositide 3-kinase: diverse roles in immune cell activation. Annu. Rev. Immunol. *22*, 563–598.

Di Cara, F., Maile, T.M., Parsons, B.D., Magico, A., Basu, S., Tapon, N., and King-Jones, K. (2015). The Hippo pathway promotes cell survival in response to chemical stress. Cell Death Differ. *22*, 1526–1539.

Di Cara, F., Sheshachalam, A., Braverman, N., Rachubinski, R., and Simmonds, A.J. (2017). Peroxisomes are required for the immune response to microbial infection. Immunity *47*, 93–106.

Di Cara, F., Bulow, M.H., Simmonds, A.J., and Rachubinski, R.A. (2018). Dysfunctional peroxisomes compromise gut structure and host defense by increased cell death and Tor-dependent autophagy. Mol. Biol. Cell *29*, 2766–2783.

Di Cara, F., Andreoletti, P., Trompier, D., Vejux, A., Bulow, M.H., Sellin, J., Lizard, G., Cherkaoui-Malki, M., and Savary, S. (2019a). Peroxisomes in immune response and inflammation. Int. J. Mol. Sci. *20*, 3877.

Di Cara, F., Rachubinski, R.A., and Simmonds, A.J. (2019b). Distinct roles for peroxisomal targeting signal receptors *Pex5* and *Pex7* in *Drosophila*. Genetics *211*, 141–149.

Di Gioia, M., Spreafico, R., Springstead, J.R., Mendelson, M.M., Joehanes, R., Levy, D., and Zanoni, I. (2020). Endogenous oxidized phospholipids reprogram cellular metabolism and boost hyperinflammation. Nat. Immunol. *21*, 42–53.

Dionne, M.S., Pham, L.N., Shirasu-Hiza, M., and Schneider, D.S. (2006). Akt and FOXO dysregulation contribute to infection-induced wasting in *Drosophila*. Curr. Biol. *16*, 1977–1985.

Dixit, E., Boulant, S., Zhang, Y., Lee, A.S., Odendall, C., Shum, B., Hacohen, N., Chen, Z.J., Whelan, S.P., Fransen, M., et al. (2010). Peroxisomes are signaling platforms for antiviral innate immunity. Cell *141*, 668–681.

Dowds, C.M., Kornell, S.C., Blumberg, R.S., and Zeissig, S. (2014). Lipid antigens in immunity. Biol. Chem. *395*, 61–81.

Eguchi, M., Sannes, P.L., and Spicer, S.S. (1979). Peroxisomes of rat peritoneal macrophages during phagocytosis. Am. J. Pathol. *95*, 281–294.

Facciotti, F., Ramanjaneyulu, G.S., Lepore, M., Sansano, S., Cavallari, M., Kistowska, M., Forss-Petter, S., Ni, G., Colone, A., Singhal, A., et al. (2012). Peroxisome-derived lipids are self antigens that stimulate invariant natural killer T cells in the thymus. Nat. Immunol. *13*, 474–480.

Faust, J.E., Verma, A., Peng, C., and McNew, J.A. (2012). An inventory of peroxisomal proteins and pathways in *Drosophila melanogaster*. Traffic *13*, 1378–1392.

Faust, P.L., and Hatten, M.E. (1997). Targeted deletion of the *PEX2* peroxisome assembly gene in mice provides a model for Zellweger syndrome, a human neuronal migration disorder. J. Cell Biol. *139*, 1293–1305.

Ferrante, A.W., Jr. (2013). Macrophages, fat, and the emergence of immunometabolism. J. Clin. Invest. *123*, 4992–4993.

Fessler, M.B., Arndt, P.G., Just, I., Nick, J.A., Malcolm, K.C., and Worthen, G.S. (2007). Dual role for RhoA in suppression and induction of cytokines in the human neutrophil. Blood *109*, 1248–1256.

Fink, C., Hoffmann, J., Knop, M., Li, Y., Isermann, K., and Roeder, T. (2016). Intestinal FoxO signaling is required to survive oral infection in *Drosophila*. Mucosal Immunol. *9*, 927–936.

Flannagan, R.S., Jaumouille, V., and Grinstein, S. (2012). The cell biology of phagocytosis. Annu. Rev. Pathol. *7*, 61–98.

Galenza, A., and Foley, E. (2019). Immunometabolism: insights from the *Drosophila* model. Dev. Comp. Immunol. *94*, 22–34.

Geng, J., Sun, X., Wang, P., Zhang, S., Wang, X., Wu, H., Hong, L., Xie, C., Li, X., Zhao, H., et al. (2015). Kinases Mst1 and Mst2 positively regulate phagocytic induction of reactive oxygen species and bactericidal activity. Nat. Immunol. *16*, 1142–1152.

Gilchrist, K.W., Opitz, J.M., Gilbert, E.F., Tsang, W., and Miller, P. (1974). Immunodeficiency in the cerebro-hepato-renal syndrome of Zellweger. Lancet *1*, 164–165.

Gross, D.N., van den Heuvel, A.P., and Birnbaum, M.J. (2008). The role of FoxO in the regulation of metabolism. Oncogene *27*, 2320–2336.

Guo, T., Gregg, C., Boukh-Viner, T., Kyryakov, P., Goldberg, A., Bourque, S., Banu, F., Haile, S., Milijevic, S., San, K.H., et al. (2007). A signal from inside the peroxisome initiates its division by promoting the remodeling of the peroxisomal membrane. J. Cell Biol. *177*, 289–303.

Harrison, D.A., McCoon, P.E., Binari, R., Gilman, M., and Perrimon, N. (1998). *Drosophila* unpaired encodes a secreted protein that activates the JAK signaling pathway. Genes Dev. *12*, 3252–3263.

Heo, W.D., Inoue, T., Park, W.S., Kim, M.L., Park, B.O., Wandless, T.J., and Meyer, T. (2006). PI(3,4,5)P3 and PI(4,5)P2 lipids target proteins with polybasic clusters to the plasma membrane. Science *314*, 1458–1461.

Heraud, C., Pinault, M., Lagree, V., and Moreau, V. (2019). p190RhoGAPs, the $ARHGAP_{35}$- and $ARHGAP_5$-encoded proteins, in health and disease. Cells *8*, 351.

Herzog, K., Pras-Raves, M.L., Vervaart, M.A., Luyf, A.C., van Kampen, A.H., Wanders, R.J., Waterham, H.R., and Vaz, F.M. (2016). Lipidomic analysis of fibroblasts from Zellweger spectrum disorder patients identifies disease-specific phospholipid ratios. J. Lipid Res. *57*, 1447–1454.

Hooftman, A., Angiari, S., Hester, S., Corcoran, S.E., Runtsch, M.C., Ling, C., Ruzek, M.C., Slivka, P.F., McGettrick, A.F., Banahan, K., et al. (2020). The immunomodulatory metabolite Itaconate modifies NLRP3 and inhibits inflammasome activation. Cell Metab. *32*, 468–478.

Hubler, M.J., and Kennedy, A.J. (2016). Role of lipids in the metabolism and activation of immune cells. J. Nutr. Biochem. *34*, 1–7.

Ishihara, S., Sato, T., Du, G., Guardavaccaro, D., Nakajima, A., Sawai, S., Kataoka, T., and Katagiri, K. (2020). Phosphatidic acid-dependent localization and basal de-phosphorylation of RA-GEFs regulate lymphocyte trafficking. BMC Biol. *18*, 75.

Jeynov, B., Lay, D., Schmidt, F., Tahirovic, S., and Just, W.W. (2006). Phosphoinositide synthesis and degradation in isolated rat liver peroxisomes. FEBS Lett. *580*, 5917–5924.

Juss, J.K., Hayhoe, R.P., Owen, C.E., Bruce, I., Walmsley, S.R., Cowburn, A.S., Kulkarni, S., Boyle, K.B., Stephens, L., Hawkins, P.T., et al. (2012). Functional redundancy of class I phosphoinositide 3-kinase (PI3K) isoforms in signaling growth factor-mediated human neutrophil survival. PLoS One *7*, e45933.

Khoo, P., Allan, K., Willoughby, L., Brumby, A.M., and Richardson, H.E. (2013). In *Drosophila*, RhoGEF2 cooperates with activated Ras in tumorigenesis through a pathway involving Rho1-Rok-Myosin-II and JNK signalling. Dis. Model. Mech. *6*, 661–678.

Khuong, T.M., Habets, R.L., Slabbaert, J.R., and Verstreken, P. (2010). WASP is activated by phosphatidylinositol-4,5-bisphosphate to restrict synapse growth in a pathway parallel to bone morphogenetic protein signaling. Proc. Natl. Acad. Sci. U S A *107*, 17379–17384.

Klein, A.T., Barnett, P., Bottger, G., Konings, D., Tabak, H.F., and Distel, B. (2001). Recognition of peroxisomal targeting signal type 1 by the import receptor Pex5p. J. Biol. Chem. *276*, 15034–15041.

Kominsky, D.J., Campbell, E.L., and Colgan, S.P. (2010). Metabolic shifts in immunity and inflammation. J. Immunol. *184*, 4062–4068.

Kural, C., Kim, H., Syed, S., Goshima, G., Gelfand, V.I., and Selvin, P.R. (2005). Kinesin and dynein move a peroxisome *in vivo*: a tug-of-war or coordinated movement? Science *308*, 1469–1472.

Kurooka, T., Yamamoto, Y., Takai, Y., and Sakisaka, T. (2011). Dual regulation of RA-RhoGAP activity by phosphatidic acid and Rap1 during neurite outgrowth. J. Biol. Chem. *286*, 6832–6843.

Lacy, P., and Stow, J.L. (2011). Cytokine release from innate immune cells: association with diverse membrane trafficking pathways. Blood *118*, 9–18.

Lai, C.L., Srivastava, A., Pilling, C., Chase, A.R., Falke, J.J., and Voth, G.A. (2013). Molecular mechanism of membrane binding of the GRP1 PH domain. J. Mol. Biol. *425*, 3073–3090.

Lam, T.K., Carpentier, A., Lewis, G.F., van de Werve, G., Fantus, I.G., and Giacca, A. (2003). Mechanisms of the free fatty acid-induced increase in hepatic glucose production. Am. J. Physiol. Endocrinol. Metab. *284*, E863–E873.

Laurinyecz, B., Peter, M., Vedelek, V., Kovacs, A.L., Juhasz, G., Maroy, P., Vigh, L., Balogh, G., and Sinka, R. (2016). Reduced expression of CDP-DAG synthase changes lipid composition and leads to male sterility in *Drosophila*. Open Biol. *6*, 50169.

Lee, K.A., Cho, K.C., Kim, B., Jang, I.H., Nam, K., Kwon, Y.E., Kim, M., Hyeon, D.Y., Hwang, D., Seol, J.H., et al. (2018). Inflammation-modulated metabolic reprogramming is required for DUOX-dependent gut immunity in *Drosophila*. Cell Host Microbe *23*, 338–352.

Lemaitre, B., and Hoffmann, J. (2007). The host defense of *Drosophila melanogaster*. Annu. Rev. Immunol. *25*, 697–743.

Levin, R., Hammond, G.R., Balla, T., De Camilli, P., Fairn, G.D., and Grinstein, S. (2017). Multiphasic dynamics of phosphatidylinositol 4-phosphate during phagocytosis. Mol. Biol. Cell *28*, 128–140.

Livak, K.J., and Schmittgen, T.D. (2001). Analysis of relative gene expression data using real-time quantitative PCR and the $2^{-\Delta\Delta C}_T$ method. Methods *25*, 402–408.

Lodhi, I.J., and Semenkovich, C.F. (2014). Peroxisomes: a nexus for lipid metabolism and cellular signaling. Cell Metab. *19*, 380–392.

Luo, L., Liao, Y.J., Jan, L.Y., and Jan, Y.N. (1994). Distinct morphogenetic functions of similar small GTPases: *Drosophila Drac1* is involved in axonal outgrowth and myoblast fusion. Genes Dev. *8*, 1787–1802.

MacIntyre, D.L., Miyata, S.T., Kitaoka, M., and Pukatzki, S. (2010). The *Vibrio cholerae* type VI secretion system displays antimicrobial properties. Proc. Natl. Acad. Sci. U S A *107*, 19520–19524.

Mao, Y., and Finnemann, S.C. (2015). Regulation of phagocytosis by Rho GTPases. Small GTPases *6*, 89–99.

Mast, F.D., Li, J., Virk, M.K., Hughes, S.C., Simmonds, A.J., and Rachubinski, R.A. (2011). A *Drosophila* model for the Zellweger spectrum of peroxisome biogenesis disorders. Dis. Model. Mech. *4*, 659–672.

Miller, R.R., Jr., Yates, J.W., and Geer, B.W. (1993). Dietary ethanol stimulates the activity of phosphatidylcholine-specific phospholipase D and the formation of phosphatidylethanol in *Drosophila melanogaster* larvae. Insect Biochem. Mol. Biol. *23*, 749–755.

Molaei, M., Vandehoef, C., and Karpac, J. (2019). NF-κB shapes metabolic adaptation by attenuating Foxo-mediated lipolysis in *Drosophila*. Dev. Cell *49*, 802–810.

Murray, R.Z., and Stow, J.L. (2014). Cytokine secretion in macrophages: SNAREs, Rabs, and membrane trafficking. Front. Immunol. *5*, 538.

Musselman, L.P., Fink, J.L., Grant, A.R., Gatto, J.A., Tuthill, B.F., 2nd, and Baranski, T.J. (2017). The relationship between immunity and metabolism in *Drosophila* diet-induced insulin resistance. Mol. Cell. Biol. *38*, e00259–17.

Nakanishi, H., de los Santos, P., and Neiman, A.M. (2004). Positive and negative regulation of a SNARE protein by control of intracellular localization. Mol. Biol. Cell *15*, 1802–1815.

Neisch, A.L., Speck, O., Stronach, B., and Fehon, R.G. (2010). Rho1 regulates apoptosis via activation of the JNK signaling pathway at the plasma membrane. J. Cell Biol. *189*, 311–323.

Nelson, R.H., Vlazny, D., Smailovic, A., and Miles, J.M. (2012). Intravenous niacin acutely improves the efficiency of dietary fat storage in lean and obese humans. Diabetes *61*, 3172–3175.

O'Donnell, V.B., Rossjohn, J., and Wakelam, M.J. (2018). Phospholipid signaling in innate immune cells. J. Clin. Invest. *128*, 2670–2679.

O'Neill, L.A., Kishton, R.J., and Rathmell, J. (2016). A guide to immunometabolism for immunologists. Nat. Rev. Immunol. *16*, 553–565.

O'Neill, L.A., and Pearce, E.J. (2016). Immunometabolism governs dendritic cell and macrophage function. J. Exp. Med. *213*, 15–23.

Palsson-McDermott, E.M., and O'Neill, L.A.J. (2020). Targeting immunometabolism as an anti-inflammatory strategy. Cell Res. *30*, 300–314.

Parsons, B., and Foley, E. (2013). The *Drosophila* platelet-derived growth factor and vascular endothelial growth factor-receptor related (Pvr) protein ligands Pvf2 and Pvf3 control hemocyte viability and invasive migration. J. Biol. Chem. *288*, 20173–20183.

Parsons, B., and Foley, E. (2016). Cellular immune defenses of *Drosophila melanogaster*. Dev. Comp. Immunol. *58*, 95–101.

Pean, C.B., Schiebler, M., Tan, S.W., Sharrock, J.A., Kierdorf, K., Brown, K.P., Maserumule, M.C., Menezes, S., Pilatova, M., Bronda, K., et al. (2017). Regulation of phagocyte triglyceride by a STAT-ATG2 pathway controls mycobacterial infection. Nat. Commun. *8*, 14642.

Pearce, E.L., and Pearce, E.J. (2013). Metabolic pathways in immune cell activation and quiescence. Immunity *38*, 633–643.

Pertea, M., Kim, D., Pertea, G.M., Leek, J.T., and Salzberg, S.L. (2016). Transcript-level expression analysis of RNA-seq experiments with HISAT, StringTie and Ballgown. Nat. Protoc. *11*, 1650–1667.

Pesta, D., and Gnaiger, E. (2012). High-resolution respirometry: OXPHOS protocols for human cells and permeabilized fibers from small biopsies of human muscle. Methods Mol. Biol. *810*, 25–58.

Pichaud, N., Ballard, J.W., Tanguay, R.M., and Blier, P.U. (2011). Thermal sensitivity of mitochondrial functions in permeabilized muscle fibers from two populations of *Drosophila simulans* with divergent mitotypes. Am. J. Physiol. Regul. Integr. Comp. Physiol. *301*, R48–R59.

Ragheb, R., Chuyen, A., Torres, M., Defaye, A., Seyres, D., Kremmer, L., Fernandez-Nunez, N., Tricoire, H., Rihet, P., Nguyen, C., et al. (2017). Interplay between trauma and *Pseudomonas entomophila* infection in flies: a central role of the JNK pathway and of CrebA. Sci. Rep. *7*, 16222.

Reimand, J., Isserlin, R., Voisin, V., Kucera, M., Tannus-Lopes, C., Rostamianfar, A., Wadi, L., Meyer, M., Wong, J., Xu, C., et al. (2019). Pathway enrichment analysis and visualization of omics data using g:Profiler, GSEA, Cytoscape and EnrichmentMap. Nat. Protoc. *14*, 482–517.

Remmerie, A., and Scott, C.L. (2018). Macrophages and lipid metabolism. Cell Immunol. *330*, 27–42.

Reversi, A., Loeser, E., Subramanian, D., Schultz, C., and De Renzis, S. (2014). Plasma membrane phosphoinositide balance regulates cell shape during *Drosophila* embryo morphogenesis. J. Cell Biol. *205*, 395–408.

Ricker, E., Chowdhury, L., Yi, W., and Pernis, A.B. (2016). The RhoA-ROCK pathway in the regulation of T and B cell responses. F1000Research *5*, 2295.

Rieger, A.M., Hall, B.E., and Barreda, D.R. (2010). Macrophage activation differentially modulates particle binding, phagocytosis and downstream antimicrobial mechanisms. Dev. Comp. Immunol. *34*, 1144–1159.

Rizki, T.M., and Rizki, R.M. (1980). Properties of the larval hemocytes of *Drosophila-melanogaster*. Experientia *36*, 1223–1226.

Ryan, D.G., and O'Neill, L.A.J. (2020). Krebs cycle reborn in macrophage immunometabolism. Annu. Rev. Immunol. *38*, 289–313.

Sadik, C.D., and Luster, A.D. (2012). Lipid-cytokine-chemokine cascades orchestrate leukocyte recruitment in inflammation. J. Leukoc. Biol. *91*, 207–215.

Salzer, E., Zoghi, S., Kiss, M.G., Kage, F., Rashkova, C., Stahnke, S., Haimel, M., Platzer, R., Caldera, M., Ardy, R.C., et al. (2020). The cytoskeletal regulator HEM1 governs B cell development and prevents autoimmunity. Sci. Immunol. *5*, eabc3979.

Schmitt, S., Ugrankar, R., Greene, S.E., Prajapati, M., and Lehmann, M. (2015). *Drosophila Lipin* interacts with insulin and TOR signaling pathways in the control of growth and lipid metabolism. J. Cell Sci. *128*, 4395–4406.

Schneider, I. (1972). Cell lines derived from late embryonic stages of *Drosophila melanogaster*. J. Embryol. Exp. Morphol. *27*, 353–365.

Schneider, C.A., Rasband, W.S., and Eliceiri, K.W. (2012). NIH Image to ImageJ: 25 years of image analysis. Nat. Methods *9*, 671–675.

Schrader, M., and Fahimi, H.D. (2006). Peroxisomes and oxidative stress. Biochim. Biophys. Acta *1763*, 1755–1766.

Seiler, F., Hellberg, J., Lepper, P.M., Kamyschnikow, A., Herr, C., Bischoff, M., Langer, F., Schafers, H.J., Lammert, F., Menger, M.D., et al. (2013). FOXO transcription factors regulate innate immune mechanisms in respiratory epithelial cells. J. Immunol. *190*, 1603–1613.

Sellin, J., Wingen, C., Gosejacob, D., Senyilmaz, D., Hanschke, L., Buttner, S., Meyer, K., Bano, D., Nicotera, P., Teleman, A.A., et al. (2018). Dietary rescue of lipotoxicity-induced mitochondrial damage in *Peroxin19* mutants. PLoS Biol. *16*, e2004893.

Simard, C.J., Pelletier, G., Boudreau, L.H., Hebert-Chatelain, E., and Pichaud, N. (2018). Measurement of mitochondrial oxygen consumption in permeabilized fibers of *Drosophila* using minimal amounts of tissue. J. Vis. Exp. https://doi.org/10.3791/57376.

Singh, J., and Aballay, A. (2017). Endoplasmic reticulum stress caused by lipoprotein accumulation suppresses immunity against bacterial pathogens and contributes to immunosenescence. mBio *8*, e00778–17.

Sit, S.T., and Manser, E. (2011). Rho GTPases and their role in organizing the actin cytoskeleton. J. Cell Sci. *124*, 679–683.

Smith, J.J., and Aitchison, J.D. (2013). Peroxisomes take shape. Nat. Rev. Mol. Cell Biol. *14*, 803–817.

Stroschein-Stevenson, S.L., Foley, E., O'Farrell, P.H., and Johnson, A.D. (2006). Identification of *Drosophila* gene products required for phagocytosis of *Candida albicans*. PLoS Biol. *4*, e4.

Szilard, R.K., Titorenko, V.I., Veenhuis, M., and Rachubinski, R.A. (1995). *Pay32p* of the yeast *Yarrowia lipolytica* is an intraperoxisomal component of the matrix protein translocation machinery. J. Cell Biol. *131*, 1453–1469.

Teng, X., Li, W., Cornaby, C., and Morel, L. (2019). Immune cell metabolism in autoimmunity. Clin. Exp. Immunol. *197*, 181–192.

Valadas, J.S., Esposito, G., Vandekerkhove, D., Miskiewicz, K., Deaulmerie, L., Raitano, S., Seibler, P., Klein, C., and Verstreken, P. (2018). ER lipid defects in neuropeptidergic neurons impair sleep patterns in Parkinson's disease. Neuron *98*, 1155–1169.

Vicente-Manzanares, M., and Sanchez-Madrid, F. (2004). Role of the cytoskeleton during leukocyte responses. Nat. Rev. Immunol. *4*, 110–122.

Vijayan, V., Srinu, T., Karnati, S., Garikapati, V., Linke, M., Kamalyan, L., Mali, S.R., Sudan, K., Kollas, A., Schmid, T., et al. (2017). A new immunomodulatory role for peroxisomes in macrophages activated by the TLR4 ligand lipopolysaccharide. J. Immunol. *198*, 2414–2425.

Volta, M., Bulfone, A., Gattuso, C., Rossi, E., Mariani, M., Consalez, G.G., Zuffardi, O., Ballabio, A., Banfi, S., and Franco, B. (1999). Identification and characterization of *CDS2*, a mammalian homolog of the *Drosophila* CDP-diacylglycerol synthase gene. Genomics *55*, 68–77.

Walter, C., Gootjes, J., Mooijer, P.A., Portsteffen, H., Klein, C., Waterham, H.R., Barth, P.G., Epplen, J.T., Kunau, W.H., Wanders, R.J., et al. (2001). Disorders of peroxisome biogenesis due to mutations in *PEX1*: phenotypes and PEX1 protein levels. Am. J. Hum. Genet. *69*, 35–48.

Wanders, R.J., and Waterham, H.R. (2006). Biochemistry of mammalian peroxisomes revisited. Annu. Rev. Biochem. *75*, 295–332.

Wangler, M.F., Chao, Y.H., Bayat, V., Giagtzoglou, N., Shinde, A.B., Putluri, N., Coarfa, C., Donti, T., Graham, B.H., Faust, J.E., et al. (2017). Peroxisomal biogenesis is genetically and biochemically linked to carbohydrate metabolism in *Drosophila* and mouse. PLoS Genet. *13*, e1006825.

Webb, A.E., Kundaje, A., and Brunet, A. (2016). Characterization of the direct targets of FOXO transcription factors throughout evolution. Aging Cell *15*, 673–685.

Wightman, P.J., Jackson, G.R., and Dipple, K.M. (2012). Glycerol hypersensitivity in a *Drosophila* model for glycerol kinase deficiency is affected by mutations in eye pigmentation genes. PLoS One *7*, e31779.

Williams, M.J. (2007). *Drosophila* hemopoiesis and cellular immunity. J. Immunol. *178*, 4711–4716.

Yan, J., and Horng, T. (2020). Lipid metabolism in regulation of macrophage functions. Trends Cell Biol. *30*, 979–989.

Yanagawa, S., Lee, J.S., and Ishimoto, A. (1998). Identification and characterization of a novel line of *Drosophila* Schneider S2 cells that respond to wingless signaling. J. Biol. Chem. *273*, 32353–32359.

Yang, H., Kronhamn, J., Ekstrom, J.O., Korkut, G.G., and Hultmark, D. (2015). JAK/STAT signaling in *Drosophila* muscles controls the cellular immune response against parasitoid infection. EMBO Rep. *16*, 1664–1672.

Yang, Y., Lee, M., and Fairn, G.D. (2018). Phospholipid subcellular localization and dynamics. J. Biol. Chem. *293*, 6230–6240.

Yeung, T., Gilbert, G.E., Shi, J., Silvius, J., Kapus, A., and Grinstein, S. (2008). Membrane phosphatidylserine regulates surface charge and protein localization. Science *319*, 210–213.

Yuan, C., Rao, R.P., Jesmin, N., Bamba, T., Nagashima, K., Pascual, A., Preat, T., Fukusaki, E., Acharya, U., and Acharya, J.K. (2011). CDase is a pan-ceramidase in *Drosophila*. Mol. Biol. Cell *22*, 33–43.

Zettervall, C.J., Anderl, I., Williams, M.J., Palmer, R., Kurucz, E., Ando, I., and Hultmark, D. (2004). A directed screen for genes involved in *Drosophila* blood cell activation. Proc. Natl. Acad. Sci. U S A *101*, 14192–14197.

Zhang, C., Wang, Y., Wang, F., Wang, Z., Lu, Y., Xu, Y., Wang, K., Shen, H., Yang, P., Li, S., et al. (2017). Quantitative profiling of glycerophospholipids during mouse and human macrophage differentiation using targeted mass spectrometry. Sci. Rep. *7*, 412.

Zmora, N., Bashiardes, S., Levy, M., and Elinav, E. (2017). The role of the immune system in metabolic health and disease. Cell Metab. *25*, 506–521.

STAR★METHODS

KEY RESOURCES TABLE

REAGENT or RESOURCE	SOURCE	IDENTIFIER
Antibodies		
Mouse peroxisomal Catalase	abcam	ab16771
Rabbit polyclonal anti SKL	Rachubinski U of A	Szilard et al., 1995
Mouse anti Rho1	the Developmental Studies Hybridoma Bank	p1D9
Mouse anti- CD11b	BioLegend	M1/70
Mouse anti- F4/80	BioLegend	BM8
Rat antibody hemagglutinin protein (HA)	Sigma-Aldrich	3F10
Mouse anti-PIP2	Enzo	ADI-915-062-100
Mouse antibody Flag M2	Sigma-Aldrich	F3165
Rabbit anti-FOXO antibody	Abcam	ab1959770
Mouse α-Tubulin	Sigma-Aldrich	T5168
Rabbit antibody Pex2	Proteintech	22163-i-AP
Mouse antibody CD3 Clone OKT3	BioLegend	317352
Mouse antibody CD4 Clone OKT4	BioLegend	317438
Mouse antibody CD19 Clone HIB19	BD	302240
Mouse antibody CD14 Clone MφP9	BD	566466
Mouse antibody CD8 Clone SK1	BD	563919
Mouse antibody CD56 Clone NCAM16.2	BD	565139
Mouse antibody IL-6 MP5-20F3	BD	MP5-20F3
Mouse antibody TNF-α	BD	MP6-XT22
Mouse antibody CD8a AF 647	Ebiosciences	53-6.7
Mouse antibody H2Kb	BioLegend	AF6-88.5
Mouse antibody CD11c	BioLegend	N418
Mouse antibody I-A/I-E	antibody I-A/I-E	N/A
Bacterial and virus strains		
mCherry-expressing E. coli	Pukatzki Stefan, U of A	MacIntyre et al., 2010
Ecc-15 (2141)	Dr. Edan Foley, U of A	Basset et al., 2000
P. entomophila	Dr. Nicolas Buchon, Cornell University.	Ragheb et al., 2017
Biological samples		
PBMC	This study	N/A
Synovial Fibroblast	This study	N/A
Chemicals, peptides, and recombinant proteins		
Lypopolysaccharides O55:B5	Sigma-Aldrich	L6529
Free Fatty Acids supplement	Sigma-Aldrich	F7050
phosphatidic acid sodium salt	Sigma-Aldrich	P9511
Nicotinic Acid	Sigma-Aldrich	481918
Pam3CSK4	InvivoGen	tlrl-pms
R848	InvivoGen	inh-cc9a
ATP	Sigma-Aldrich	A1852
Rhosin (Merck),	Sigma-Aldrich	555460-M
EHop-016	Sigma-Aldrich	SML0526-5MG
Rho/Rac activator I	Cytoskeleton	#CN04

(*Continued on next page*)

Continued

REAGENT or RESOURCE	SOURCE	IDENTIFIER
Critical commercial assays		
Proteome Profiler Mouse Cytokine Array Kit	R&D Systems	ARY006
Mouse IL-6 ELISA assays	Invitrogen, Thermo Fisher	KMC0061
Mouse IL-1β ELISA assays	Invitrogen, Thermo Fisher	BMS6002
Mouse mouse TNF-α	Invitrogen, Thermo Fisher	BMS607-3
RhoA G-LISA assay	Cytoskeleton	Bk124
Rac1 G-LISA assay	Cytoskeleton	Bk126
NEB Next Ultra RNA library prep kit for Illumina	NEB	E7530S
PIP3 ELISA Kit	Echelon bioscience	K-2500S
Total Phosphatidic Acid Assay Kit	Cell Biolabs, INC	MET-5019
Free Fatty Assay Kit	Sigma-Aldrich	MAK044-1KT
Deposited data		
RNAseq data ncbi accession number	This study	PRJNA777287; https://www.ncbi.nlm.nih.gov/sra/PRJNA77728
Experimental models: Cell lines		
Drosophila melanogaster S2R+	DGRC	Stock Number: 150
Drosophila melanogaster Pex1 mutant S2R+	This study	N/A
Mouse: Bone marrow derived macrophages from Sw129-*Pxmp3*^{tm1Plf}-/-	Mutant Mouse Resource and Research Centre (MMRRC) supported by the NIH	Faust and Hatten, 1997
Mouse: Bone marrow derived macrophages from Sw129-*Pxmp3*^{tm1Plf}-/+	MMRRC	Faust and Hatten, 1997
Experimental models: Organisms/strains		
Drosophila melanogaster: RNAI lines y^{1} v^{1}; P{TRiP.HMC04009}attP40	Bloomington Drosophila Stock Center	#55322
W^{1118}	King-Jones, U of A Di Cara et al., 2015	N/A
hml-GAL4, UAS-GFP, Dpt-GFP	Foley, U of A	N/A
P{y[+t7.7] v[+t1.8]=TRiP.JF02912}attP2	Bloomington Drosophila Stock Center	28075
P{Ubi-GAL4.U}2/CyO	Bloomington Drosophila Stock Center	32551
P{UAS-Rho1.N19}2.1	Bloomington Drosophila Stock Center	7328
P{UAS-Rho1.V14.E40L}4	Bloomington Drosophila Stock Center	7332
P{UAS-Rac1.N17}1	Bloomington Drosophila Stock Center	6292
P{w[+mC]=UAS-Rac1.V12	Bloomington Drosophila Stock Center	6291
M{w[+mC]=UAS-hDGK.}ZH-86Fb	Bloomington Drosophila Stock Center	65800
UAS-Upd3-GFP	Harrison, University of Kentucky Harrison et al., 1998	N/A
Act5C-GAL4/CyO	King-Jones, U of A Di Cara et al., 2015	N/A
UAS-FOXO	King-Jones, U of A Di Cara et al., 2015	N/A
UAS-GFP	King-Jones, U of A Di Cara et al., 2015	N/A
129S6.129-Pex2^{tm1Plf}*/Mmmh*	Mutant Mouse Resource and Research Centre Faust and Hatten, 1997	N/A
Swiss Webster	Charles River	024
Oligonucleotides		
see Table S4		N/A

(*Continued on next page*)

Continued

REAGENT or RESOURCE	SOURCE	IDENTIFIER
Recombinant DNA		
pAHWRhoI^{N19}	Fehon, University of Chicago	Neisch et al., 2010
pAHWRhoI^{V14}	Fehon, University of Chicago	Neisch et al., 2010
and pAFW Rac1^{V12}	Fehon, University of Chicago	Neisch et al., 2010
pAGW-GRP1-GFP	This study	N/A
pAW- Lact C2-GFP	This study	N/A
pAW-PABD-RFP	This study	N/A
pAW-*Rok*	This study	N/A
pAW- *PI3K92E*	This study	N/A
pAW- *CdsA*	This study	N/A
pAW-Rho GAP p190	This study	N/A
Software and algorithms		
IDEAS software	Millipore	N/A
Imaris 8.3.1	Bitmap	N/A
MegaView III Soft Imaging System	Olympus	N/A
FIJI/imageJ software	Schneider et al., 2012	https://imagej.nih.gov/ij/
GraphPad 6	Prism	N/A
HISAT2, StringTie, Ballgown and Deseq2 pipeline	NA	Pertea et al., 2016
Cytoscape	NA	Reimand et al., 2019
Icy Bioimage	BioImage Analysis Lab at Institut Pasteur	http://icy.bioimageanalysis.org
FloJo	BD	N/A
Zeiss Zen lite Black & lite Blue	Zeiss	https://www.zeiss.com/microscopy/int/products/microscope-software/zen-lite.html?vaURL=www.zeiss.com/zen-lite
Other		
Double strand RNA library	Rnai-UCSF	Stroschein-Stevenson et al., 2006

RESOURCE AVAILABILITY

Lead contact

Further information and requests for resources and reagents should be directed to and will be fulfilled by the lead contact, Francesca Di Cara (dicara@dal.ca).

Materials availability

- Plasmids made in this study are available from the lead contact upon request.
- The cell lines made in this study are available from the lead contact upon request.
- No new mouse or *Drosophila* line was made in this study.

Data and code availability

- RNA-seq data have been deposited at GEO and are publicly available as of the date of publication. Accession numbers are listed in the key resources table. Microscopy data reported in this paper will be shared by the lead contact upon request.
- Any additional information required to reanalyze the data reported in this paper is available from the lead contact upon request.
- This paper does not report original code.

EXPERIMENTAL MODEL AND SUBJECT DETAILS

Any additional information required to reanalyze the data reported in this paper is available from the lead contact upon request.

Fly cell culture

S2R+ cells (Yanagawa et al., 1998) were obtained from the Drosophila Genomics Resource Center. *Pex1* S2 cells were made using S2R+ cells. *Pex1* S2 cells expressing GFP-SKL were made using S2 cells expressing GFP-SKL, a kind gift from Dr. Ronald Vale,

University of California San Francisco (Kural et al., 2005). All cells were grown in SFM4 Insect Cell Culture Medium (GE Biosciences) supplemented with 50 U penicillin/mL and 50 μg streptomycin sulfate/mL. CRISPR/Cas9-derived *Pex1* S2 cell lines were made as described previously (Bassett et al., 2014). The guide RNA sequences cloned to target the *Pex1* gene are 5'-TTCGATCCGGTCG-CATTGATCGCTTGG and 5'-AACCCAAGCGATCAATGCGACCGGAT.

All S2 cell lines were derived from *Drosophila melanogaster* male embryos, according to protocols from the Drosophila Genomics Resource Center (DGRC). Indel mutations in the genomic DNA of pre-selected clones were confirmed by fragment length analysis of the amplified locus that was targeted by *Pex1* sgRNA. We used double-stranded RNA-mediated RNA interference (dsRNAi) to generated cells depleted of each gene of interest, including *Pex5*-i cells that have defects in peroxisome biogenesis and function and were used in the transcriptomic and lipidomic analyses. All dsRNA interference treatments of cell cultures were done using the *Drosophila* RNA interference library and protocol described previously (Stroschein-Stevenson et al., 2006). Gene depletions were verified by qRT-PCR to verify the strength of each relevant double-stranded RNA (Figures S7G and S7H).

Fly stocks, husbandry and microinjection

Pex5 dsRNA-expressing lines y^1 v^1; *P{TRiP.HMC04009}attP40* and w^{1118}; *P{GD14972}v42332* were from the Bloomington Drosophila Stock Center (BDSC). The *CdsA* dsRNA-expressing line *P{y[+t7.7] v[+t1.8]=TRiP.JF02912}attP2* was from the Vienna Drosophila Resource Center. The ubiquitous driver line P{Ubi-GAL4.U}2/CyO (32551) and the cDNA expressing lines *P{UAS-Rho1.N19}2.1*(7328), *P{UAS-Rho1.V14.E40L}4* (7332), *P{UAS-Rac1.N17}1* (6292), *P{w[+mC]=UAS-Rac1.V12}* (6291) and *M{w[+mC]=UAS-hDGKG.HA}ZH-86Fb* (65800) were from the BDSC. The line expressing *UAS-Upd3-GFP* was a gift from Dr. Douglas Harrison, University of Kentucky (Harrison et al., 1998). The plasmatocyte-specific driver *Hml-GAL4*, *UAS-GFP* strain was a gift from Dr. Edan Foley, University of Alberta (Parsons and Foley, 2013). The *Act5C-GAL4/CyO*, *UAS-FOXO* and *UAS-GFP* strains were gifts from Dr. Kirst King-Jones, University of Alberta (Di Cara et al., 2015).

Drosophila strains were cultured at 25°C on standard BDSC cornmeal medium supplemented with soy powder. For oral infection, flies were cultured on filter paper soaked in 5% sucrose or 5% sucrose containing *Ecc15* (OD_{600} = 200) or *E. coli* (OD_{600} = 200). Flies were transferred to fresh vials every 2 days, and the number of dead flies was determined daily.

For infection by microinjection, flies were microinjected into the thorax using 1-μm internal diameter, thin-walled glass needle pulled with a P-97 Flaming/Brown micropipette puller (Sutter) mounted on a PV830 microinjector and needle positioner (World Precision Instruments). Each adult fly was injected with 4 nL of *Ecc15* (OD_{600} = 200) or *Pseudomonas entomophila* (OD_{600} = 25) in phosphate buffered saline (PBS) or PBS alone (control). Survival experiments were done with a total of 200 flies for each group. Injected flies were transferred to 29°C, and the number of dead flies was determined every 2 days.

To generate survival curves for flies with knock downs of *Pex* genes exclusively in plasmatocytes (*Hml*-driven knock down), adult flies were anesthetized with CO_2 and infected by being pricked in the thorax with a thin needle that had been dipped into bacterial working solution. Survival experiments were done at 29°C with 20-30 flies for each group. Surviving flies were transferred daily to fresh vials and counted.

For extraction of plasmatocytes from adults, anesthetized flies were cut into 3 parts with surgical forceps (Fine Science Tools, Dumont #55 Forceps) and allowed to bleed for 1 min into a glass dish filled with 100 mL of SFM4 Insect Cell Culture Medium containing cOmplete™ Protease Inhibitor Cocktail (Roche) to avoid coagulation. The cell suspension was filtered on 70-μm microcentrifuge filters and processed for immunofluorescence in an 8-chamber cover glass (Nunc).

All experiments were conducted using an equal number of 3-4 day-old male and female adult *D. melanogaster* flies.

Mammalian cells

Murine bone marrow-derived macrophages

Murine bone marrow-derived monocytes were extracted from male and female 1-day-old pups, differentiated to macrophages (BMDMs) and treated as previously described (Geng et al., 2015).

Human peripheral blood mononuclear cells

Peripheral blood mononuclear cells (PBMCs) from 9-year-old healthy males and from aged-matched male patients affected by Kawasaki Disease were provided by Dr. Beata Derfalvi, IWK Health Centre, Dalhousie University (IWK REB#: 1020232). Frozen cell stocks were thawed and grown in RPMI medium (Gibco) supplemented with 10% heat-inactivated fetal bovine serum (HI FBS) (Hyclone, Thermo Scientific), 2 mM *L*-glutamine (Gibco), 50 mM 2-mercaptoethanol, 50 U penicillin/mL, 50 μg streptomycin sulfate/mL. PBMCs were grown in the absence or presence of 200 ng LPS from *E. coli* O55:B5 (Sigma-Aldrich)/mL or in the presence of a proinflammatory cytokine cocktail (IL-6, IL-1β and TNFα, each at 10 μg/mL) for 24 h. Cells were harvested and stained for flow cytometry analysis or immunofluorescence microscopy.

Human synovial fluid fibroblasts

Synovial fluid fibroblasts (SFFs) from 4-year old healthy females and from aged-matched female patients affected by Juvenile Idiopathic Arthritis were provided by Dr. Beata Derfalvi, IWK Health Centre, Dalhousie University (IWK REB#: 1020232). Frozen cell stocks were thawed and grown in MEM-α (Gibco) medium supplemented with 20% HI FBS, 1 mM sodium pyruvate, 1X MEM

NEAA (Gibco), 2 mM *L*-glutamine, 50 mM 2-mercaptoethanol, 50 U penicillin/mL, 50 μg streptomycin sulfate/mL. Cells were grown for 24 h, harvested and processed for immunofluorescence microscopy.

Bacteria

mCherry-expressing *E. coli* was a kind gift of Dr. Stefan Pukatzki, University of Alberta (MacIntyre et al., 2010). The bacteria were grown in LB broth at 37°C for 16 h. *Ecc15* was a kind gift of Dr. Edan Foley, University of Alberta. The bacteria were grown in LB broth at 29°C for 24 h. *P. entomophila* was a kind gift of Dr. Nicolas Buchon, Cornell University. The bacteria were grown in LB broth at 29°C for 24 h.

Pex2 mutant mice

The *Pex2* mutant mouse strain used was 129S6.129-*Pex2*^{tm1Plf}/Mmmh (null allele) (Faust and Hatten, 1997) and was obtained from the Mutant Mouse Resource & Research Centers (MMRRC) supported by the National Institutes of Health. The mice used for the experiments reported herein were *Pex2*$^{+/+}$, *Pex2*$^{-/-}$ and *Pex2*$^{+/-}$. Homozygous null mutants showed no *Pex2* transcript and no Pex2 protein. Homozygous null mutants in the congenic strain 129S6.129-*Pex2*^{tm1Plf} +/- showed variable embryonic lethality, starting at ~E11. Approximately 20% of homozygous null mutants survived to birth but were hypotonic, did not feed, and died on the day of birth. Homozygous null mutant mice that survived into the postnatal period were obtained by mating congenic 129S6.129-*Pex2*^{tm1Plf} +/- mice with wild-type Swiss Webster strain mice. F1-*Pxmp3*^{tm1Plf}+/- hybrids (designated Sw129) were then intercrossed to obtain Sw129-*Pxmp3*^{tm1Plf}-/- (indicated in the text as *Pex2*$^{-/-}$) mice.

Colonies were maintained as stable inbred lines in the Swiss Webster and 129SVEV backgrounds under approved animal protocol #19-002, abiding by the standards of the Canadian Council on Animal Care.

METHOD DETAILS

Reagents

Mouse antibody to peroxisomal catalase (ab16771), and Alexa Fluor 488-conjugated and Alexa Fluor 555-conjugated donkey anti-mouse or donkey anti-rabbit secondary antibodies were from Abcam. Rabbit anti-SKL antibodies have been described (Szilard et al., 1995). Antibody to Rho1 (p1D9) was developed by Dr. Susan Parkhurst, Fred Hutchison Cancer Research Center, and was obtained from the Developmental Studies Hybridoma Bank. Rat antibody to hemagglutinin protein (HA), clone 3F10, was from Roche. Mouse anti-PIP2 antibody (ADI-915-062-100) was from Enzo. Mouse monoclonal antibody (F1804) to anti-Flag M2 antibody was from Sigma-Aldrich. Mouse antibody to α-tubulin (T5168) was from Sigma-Aldrich. Rabbit anti-FOXO antibody (ab1959770) was from Abcam.

Cy5 fluorescently labeled anti-CD11b (M1/70) or anti-F4/80 (BM8) antibodies were from BioLegend. Rabbit antibody to Pex2 (22163-i-AP) was from Proteintech. Mouse fluorescently labeled antibodies to CD3 (Clone OKT3, Cat. no. 317352) and CD4 (Clone OKT4, Cat. no. 317438) were from BioLegend. Mouse fluorescently labeled antibodies to CD19 (Clone HIB19, Cat. no 302240), CD14 (Clone MφP9, Cat. no. 566466), CD8 (Clone SK1, Cat. no. 563919), CD56 (Clone NCAM16.2, Cat. no. 565139) IL-6 (Clone MP5-20F3) and TNF-α (Clone MP6-XT22) were from BD Biosciences. Fluorescently labeled mouse antibody CD8a AF 647 (Clone 53-6.7) was from eBioscience. Fluorescently labeled mouse antibodies H2Kb (Clone AF6-88.5) and CD11c (Clone N418) were from BioLegend. Fluorescently labeled antibody I-A/I-E (Clone M5/114.15.2) was from Becton Dickinson.

Macrophage treatment with Rho GTPase inhibitors and activator

Murine WT and Pex2$^{-/-}$ BMDMs were treated before LPS stimulation with 40 mM RhoA inhibitor, Rhosin (Merck), or GTPase inhibitor, EHop-016 (Sigma-Aldrich), for 40 min, and tested for GTPase activation, cytoskeleton rearrangement, or cytokine secretion by G-LISA, immunofluorescence microscopy, or ELISA, respectively. Murine WT and Pex2$^{-/-}$ BMDMs were treated before LPS-stimulation with 5 μg Rho/Rac activator I (CN04, Cytoskeleton, Inc.)/mL for 3 h and tested for cytoskeleton remodeling by immunofluorescence microscopy.

Treatment of murine BMDMs with fatty acids, phosphatidic acid, and niacin

Murine WT BMDMs were treated for 24 h with 2% Fatty Acid Supplement (Sigma-Aldrich, F7050) or with 50 μM phosphatidic acid sodium salt (Sigma-Aldrich) for 1 h prior to stimulation with LPS. Cells were then analyzed for cytoskeleton remodeling by immunofluorescence microscopy or cytokine secretion by ELISA. Pex2$^{-/-}$ BMDMs were treated with 100 mM niacin for 48 h prior to stimulation with 100 ng LPS/mL. Cells were then analyzed for cytoskeleton remodeling by immunofluorescence microscopy or cytokine secretion by ELISA.

Treatment of murine BMDMs with lipopolysaccharides, Pam3CSK4 and R848, and cytokine detection and measurements

Murine WT and Pex2$^{-/-}$ BMDMs were plated at a density of 10^5 cells per well in 24-well plates. Half of the cells were stimulated for 9 h with 100 ng LPS/mL, while the other half were left as unstimulated controls. Various cytokines were detected using the Proteome Profiler Mouse Cytokine Array Kit, Panel A (R&D Systems, ARY006) following the manufacturer's instructions. Secretion of selected

proinflammatory cytokines (IL-6, IL1-β, TNF-α) was assessed using mouse IL-6, Mouse IL-1β and mouse TNF-α ELISA assays (Invitrogen, Thermo Fisher). To test for IL-1β secretion, BMDMs were treated with 5 mM ATP for 1 h after 24 h of LPS treatment. WT and Pex2$^{-/-}$ BMDMs were also stimulated for 24 h with 10 ng Pam3CSK4 (InvivoGen)/mL or 100 ng R848 (InvivoGen)/mL and tested for IL-6 secretion by ELISA assay. ELISA assays were carried out following the manufacturer's instructions (Invitrogen, Thermo Fisher).

Constructs

Vectors pAHWRho1, pAHWRho1N19, pAHWRho1V14 and pAFWRac1V12 (Neisch et al., 2010) used to transfect S2 cells were kind gifts of Richard Fehon, University of Chicago.

GRP1-GFP was made by first amplifying the cDNA sequence coding for the pleckstrin homology domain of the general receptor for phosphoinositides, isoform 1, from nucleotides 779-1188 using primers GRP1-Forward 5'-CACCGGCCTCTGCTCGCCGTGCCC GGG and GRP1-Reverse 5'-AAACTACAGCTGGCTCTCCTCCTCC. The amplified fragment was cloned into the pENTR/D-TOPO donor vector (Thermo Fisher) and then transferred to the *Drosophila* Gateway destination vector, pAGW.

pLactC2-GFP was made by amplifying the Lact2-GFP fusion coding region using the primers EGFP-Forward 5'-CAACATGGT-GAGCAAGGGCGAGGAGCTGTT and LactC2-Reverse 5'-GCAGACGAATTCCTAACAGCCCAGCAGCTCC from the vector pEG FP-C1-LactC2 (Yeung et al., 2008), kindly donated by Sergio Grinstein, University of Toronto. The amplified fragment was cloned into the pENTR/D-TOPO donor vector and then transferred to the destination vector, pAW.

A vector expressing red fluorescent protein (RFP) fused to a PA-binding domain (PABD-RFP) was made by amplification of the sequence for the PA-binding domain from the *SPO20* gene encoding *Saccharomyces cerevisiae* sporulation-specific protein 20 (ORF Clone: SPO20_OSi04016D_pcDNA3.1+/ C-(K)-DYK, GenEZ) using primers PABD-Forward 5'-CAACATGGACAATTGTTCAG-GAAGCAGAA and PABD-Reverse 5'-AAAACTAGTCTTAGTGGCGTCATC. The amplified fragment was cloned in the pENTR/D-TOPO donor vector and then transferred to the *Drosophila* Gateway destination vector, pARW.

The *Drosophila Rock* cDNA catalytic domain was amplified from genomic DNA extracted from transgenic fly *P{UAS-Rok.CAT}7.1* expressing the sequence for the Rock catalytic domain under *UAS* control. The 1454-bp long *Rock* coding region was amplified using the primers Rock Forward 5'-CACCATGCCAGCTGGACGAGAAACTGT and Rock Reverse 5'-CTAGGAATTCGACGGCCGATGG. The amplified fragment was cloned into the pENTR/D-TOPO donor vector and then transferred to the destination vector, pAW.

The *Drosophila* recombinant vector PI3K92E was made by amplification of the clone FMO08840 obtained from the Drosophila Genomic Research Center (DGRC) using primers PI3K92E Forward 5'-CCACATGAACATGATGGACAACCG and PI3K92E Reverse 5'-TTACTGTTTGTTGTTTTTGGAGAAG. The amplified fragment was cloned into the pENTR/D-TOPO donor vector and then transferred to the destination vector, pAW.

The *Drosophila Pis* recombinant vector was made by amplification of cDNA clone RE35104 from the DGRC using primers Pis Forward 5'- CCACATGACAATTGCCGAGCACGATAAC and Pis Reverse 5'-AAATCACTCCACTTTCTTGCC. The amplified fragment was cloned into the pENTR/D-TOPO donor vector and then transferred to the destination vector, pAW.

The *Drosophila CdsA* recombinant vector was generated by amplification of cDNA clone FI18858 obtained from the DGRC using primers CdsA Forward 5'- CCACATGGCCGAAGTGCGACGCA and CdsA Reverse 5'-TTAGGTTAACATGTCGCCCAAG. The amplified fragment was cloned into the pENTR/D-TOPO donor vector and then transferred to the destination vector, pAW.

The *Drosophila* RhoGAPp190 recombinant vector was made by amplification of clone RE1088 using primers p190GAP Forward 5'-ACCATGCGTCAGTTTAACATCTCG and p190GAP Reverse 5'-AAAGACCATGACAAAAGCATC. The amplified fragment was cloned into the pENTR/D-TOPO donor vector and then transferred to the destination vector, pAGW, for expression of RhoGAPp190-GFP.

Assay for Rho GTPase activation

The amounts of activated (GTP-bound) RhoA and Rac1 were measured in resting, bacterially infected or LPS-stimulated cells by G-LISA, an ELISA-based assay that quantifies the amount of the active GTP-bound form of Rac1 and Rho1, according to the manufacturer's protocol (Cytoskeleton). Briefly, cells were grown in 24-well plates at a density of 10^5 cells/well. Half of the wells were stimulated with 20 ng LPS/mL (murine macrophages) or *Ecc15* (S2 cells) for 20 min, while the other half were left as untreated controls. Cells were then lysed in the buffers provided by the manufacturer, centrifuged to remove debris, and equivalent amounts of supernatant were incubated in 96-well microtiter dishes precoated with probes that specifically recognize the activated forms of RhoA and Rac1. Constitutively active forms of Rho proteins provided by the manufacturer were used as positive controls. After incubating for 30 min, wells were washed and incubated with primary antibodies that recognize RhoA or Rac1, followed by an HRP-conjugated secondary antibody. The amounts of activated RhoGTPase proteins were determined by the luminescence intensity of the HRP reagent using a Spectramax 190 microplate reader (Molecular Devices).

Lipidomics

Lipid extraction, analysis, identification and quantification were performed at the Core Facility Metabolomics, Laboratory Genetic Metabolic Diseases, University of Amsterdam, essentially as described (Herzog et al., 2016).

Heatmaps

Heatmaps of the most important lipid changes between different groups were generated by calculating the *Z*-score of each individual sample in the screen, where Z = (X (value of the individual sample) - μ (average of the row) / σ (standard deviation of the row)).

RNA-seq

For RNA-seq, 4 independent biological replicates of cells of the indicated genotype and under the indicated condition were analyzed. Total RNA was extracted using TRIzol reagent (Thermo Fisher) and the Rneasy Micro Kit (Qiagen) and then depleted for rRNA using RiboZero (Illumina). RNA quality was determined using the RNA 6000 Pico Kit (Agilent) and an Agilent 2100 Bioanalyzer. Libraries were prepared using the NEBNext Ultra RNA Library Prep Kit for Illumina (New England Biolabs) and NEBNext Multiplex Oligos for Illumina (Index primers). 2-nM libraries were analyzed using the MiSeq Reagent Kit V2 (500 cycles) (paired-end reads, 2 x 150 cycles) at The Applied Genomics Core (TAGC), University of Alberta. RNA-seq data were analyzed using the HISAT2, StringTie, Ballgown and Deseq2 pipeline, as reported previously (Pertea et al., 2016). Gene expression profile changes between control S2 cells and *Pex5*-i cells under an indicated condition were analyzed using Gene Set Enrichment Analysis to identify biological processes, cellular components, and KEGG pathways that were differentially regulated in the absence of functional peroxisomes. Data from the Gene Set Enrichment Analysis were then visualized using GeneMANIA Force-Directed Layout of the Enrichment Map plugin in Cytoscape to generate the gene interaction network (Reimand et al., 2019). The resulting network map was curated to remove redundant and uninformative nodes, resulting in a simplified network. The maps for each comparison were combined.

RNA extraction and qRT-PCR

Cells or adult flies were rinsed twice with PBS, transferred to TRIzol reagent, and snap-frozen in liquid nitrogen. Total RNA was extracted using the Rneasy Micro Kit, according to the supplied protocol. RNA was reverse transcribed using 1) the iScript cDNA Synthesis Kit (Bio-Rad), and the synthesized cDNA was used for qPCR using the SYBR-Green PCR master mix (i-SYBR) (Bio-Rad) and a CFX qPCR machine (Bio-Rad) or 2) an oligo-dT_{18} primer and SuperScript III Reverse Transcriptase (Thermo Fisher), and the synthesized cDNA was used for q-PCR using the Maxima SYBR Green/ROX qPCR Master Mix (Thermo Fisher) and a QuantStudio 6 Flex Real-Time PCR system (Applied Biosystems). Samples were normalized to *rpl23* gene expression for *Drosophila* experiments or to *Hprt* gene expression for mouse experiments using the $2^{-\Delta\Delta C}{}_T$ method (Livak and Schmittgen, 2001). Primer sequences used in qRT-PCR are presented in Table S4.

Mitochondrial respiration rate

Mitochondrial oxygen consumption in both intact and permeabilized cells was measured at 25°C (Pesta and Gnaiger, 2012) using a high-resolution respirometer (Oxygraph O2K, Oroboros Instruments, Innsbruck, Austria). Cells were counted by flow cytometry (Attune NxT, Thermo Fisher) by standard forward scatter (FSC) and size scatter (SSC) approaches and then collected by centrifugation at 250 x *g* for 5 min. The cell pellet was then resuspended in a respiration medium optimized for *Drosophila* consisting of 120 mM KCl, 5 mM KH_2PO_4, 3 mM HEPES, 1 mM EGTA, 1 mM $MgCl_2$, 0.2% BSA, pH 7.2 (Pichaud et al., 2011; Simard et al., 2018) at a concentration of 250,000 cells/mL. Cells (N = 3 for each cell line) were then transferred to the chambers of the oxygraph filled with oxygen-saturated respiration medium. After stabilization of the signal, the routine respiration rate, which represents the mitochondrial oxygen consumption of intact cells with endogenous substrates, was measured (Pesta and Gnaiger, 2012). Titration of digitonin was then done by steps of 5 μg/mL to permeabilize the plasma membrane of cells (optimal concentration of 20 μg/mL) and to allow oxidative substrates to reach the mitochondria. Addition of pyruvate (10 mM), malate (2 mM), proline (10 mM), glycerol-3-phosphate (15 mM) and ADP (5 mM) allowed coupling of the electron transport from complex I, proline dehydrogenase and mitochondrial glycerol-3-phosphate dehydrogenase to the phosphorylation of ADP to ATP, and measured the OXPHOS respiration rate. This substrate mixture was optimized and reflects the main oxidative substrates used by *Drosophila* mitochondria (Simard et al., 2018). Titration of FCCP (steps of 0.25 μM) was then done to evaluate the non-coupled respiration (ETS respiration rate), which represents the electron transport system maximal capacity (optimal concentration of 0.75 μM). Subsequently, additions of rotenone (0.5 μM) and antimycin A (2.5 μM) allowed the inhibition of complexes I and III and measured the residual oxygen consumption due to non-mitochondrial oxidative side reactions (Pesta and Gnaiger, 2012), which was subtracted from the other respiration rates. Finally, TMPD (0.5 mM) and ascorbate (2 mM) were injected to measure the maximal capacity of complex IV. Auto-oxidation of TMPD was corrected after injection of sodium azide (100 mM) to inhibit complex IV. All respiration rates are presented as pmol of $O_2.s^{-1}.10^6$ $cells^{-1}$.

Bacterial burden and survival rate of adult flies

Bacterial burden of infected adult flies and survival rate of adult flies were determined as described (Di Cara et al., 2017).

Isolation of cell membranes

Cells were isolated in 0.25 M STKM buffer (0.25 M sucrose, 25 mM HEPES-KOH, pH 7.4, 25 mM KOAc, 5 mM $MgCl_2$, 0.1 mM EDTA, 1 x Complete Protease Inhibitor (Roche), 1 mM DTT) and sonicated in a sonicator bath to yield lysates. Lysates were centrifuged at 1,000 x *g* for 10 min at 4°C. The supernatant from this first spin was centrifuged at 10,000 x *g* for 20 min at 4°C. The supernatant from this second spin and containing fragmented membranes was then centrifuged at 100,000 x *g* at 4°C for 1 h. The resultant pellets were resuspended in 0.25 M STKM and used for lipid assays.

Quantification of FFAs, PA and PIP3

PIP3 quantification was done using the PIP3 Mass ELISA Kit (Echelon Biosciences). PA quantification was done using the Total Phosphatidic Acid Assay Kit (Cell Biolabs). FFA quantification was done using the Free Fatty Assay Kit (Sigma). All assays were done following the manufacturers' protocols.

Lipid amounts were normalized to cell number or protein amount.

Immunofluorescence microscopy

Cells were fixed in 4% paraformaldehyde in PBS for 30 min, and then incubated for 1 h at room temperature in 5% normal goat serum in 1x PBS and for 16 h at 4°C with primary antibody at a 1:100 dilution in 5% normal goat serum in 1x PBS. Appropriate Alexa Fluor secondary antibodies were then used at 1:1000 dilution in 5% normal goat serum, while Cy5 fluorescently labeled phalloidin was added to stain the cytoskeleton. After 4 washes in PBST (PBS + 0.1% (v/v) Triton X-100), cells were mounted in DAPI Pro-Gold Antifade Reagent (Thermo Fisher) and imaged using a 100x oil immersion objective (NA = 1.4) mounted on an AxioObserver M1 microscope (Zeiss) or using a Zeiss AxioObserver LSM 880 Airyscan, 100x 1.4 oil plan-Apochromat lens. Alternatively, unmounted cells were imaged while submerged in a Nunc 155411 chambered borosilicate cover glass chamber (Thermo Fisher) or glass cover glass chamber (ibidi).

Live-cell imaging

Cells were imaged while submerged in a μ-8 well glass bottom chambered cover glass chamber (ibidi). Images were captured every min over 60 min using a Zeiss LSM 880 confocal microscope and a Plan-APOCHROMAT 100x/1.4 Oil DIC lens. Videos were processed using Icy Bioimage analysis software (http://icy.bioimageanalysis.org).

Flow cytometry

Flow cytometry of human PBMCs was performed as follows. PBMCs removed of red blood cells by treatment with Ammonium-Chloride-Potassium (ACK) lysis buffer (8.02 g NH_4Cl/L, 1.0 g $KHCO_3$/L 37 mg $Na_2EDTA \cdot 2H_2O$/L) were counted and resuspended in FACS buffer (0.5% BSA in sterile, filtered PBS) prior to staining. PBMCs were first surface-stained for 30 min on ice with antibodies (1:100 dilution) targeted against human CD3, CD4, CD8, CD14, CD19 and CD56. Subsequently, PBMCs were stained intracellularly with anti-SKL antibody (1:200 dilution). Post-acquisition, after gating out doublets and cell debris, PBMCs were separated as reported previously (Cliff et al., 2019). PBMCs were first separated based on CD3 and CD14 expression to isolate the monocyte/macrophage fraction. The CD3 positive cells were further subdivided into CD4- and CD8-expressing T-cells. CD3 and CD14 negative cells were then subdivided into B-cells based on CD19 expression and into two NK-cell subpopulations (bright and dim) based on CD56 expression. Presence of anti-SKL antibody signal was then determined for monocytes/macrophages, CD4 and CD8 positive T-cells, CD19 expressing B-cells, and CD56 dim and bright NK-cells.

Multi-spectral imaging flow cytometry (IFC)

To perform IFC, 10^{10} mCherry-expressing *E. coli* cells were added to 10^9 S2 cells, and the combined cells were incubated for 15 min at 4°C to allow for *E. coli* cell-S2 cell contact and then incubated for 2 h at 25°C in SFM4-Insect Cell Culture Medium. DNA was detected by staining with Hoechst 33342. Data were acquired on an ImageStream Imaging Flow Cytometer (Amnis) (Rieger et al., 2010). Cells were analyzed *post hoc*.

Internalization assay

The number of mCherry+ S2 cells was determined for each population by comparing the percentage of cells with internalized mCherry-*E. coli* to the percentage of cells with surface-bound mCherry-*E. coli*. Using IDEAS software (Millipore), a mask was created to identify the eukaryotic cell membrane using the bright field signal for two sets of samples and cell tracker dye for two other sets of samples. This allowed differentiation between internalized (degree of internalization greater than 0) and bound (degree of internalization less than 0) mCherry particles in the *x-y* axes and in the *z*-axis.

QUANTIFICATION AND STATISTICAL ANALYSIS

Statistical analysis

Prism was used to generate graphs and quantify p values using statistical methods as indicated in the respective figure legends. Tests, numbers of experiments, error bars and meaning of p values are indicated in each figure legend.

Quantification of cell area defined by phalloidin staining

We measured the cell area defined by phalloidin staining for each cell in a region of interest. Cells falling in the defined pixel threshold were counted as positive.

To determine the intensity of the defined cells within the image:

1) – Open image.

File -> Open…
2) – Select image type.
Image -> type -> 8-bit
3) – Analysis
Analyze -> Set Measurements -> Check the boxes: area, perimeter and intensity
4) – Draw a region of interest:
Select rectangle -> select a region of interest (ROI) around a cell
5) – Analysis
Analyze -> Measure
6) Repeat 4 and 5 for every cell in a frame in each biological replicate for each genotype and under each condition.

Infected S2 cells with cortical cytoskeleton defects presented an area value between 20,000 and 50,000 pixels, while control S2 cells presented an area value between 60,000 and 200,000 pixels. Murine macrophages with cytoskeleton defects presented an area value between 40,000 and 250,000 pixels, while control murine macrophages presented an area value between 270,000 and 400,000 pixels.

Quantification of signaling molecule location

Software used: Icy Bioimage Analyser (http://icy.bioimageanalysis.org/), Zeiss Zen lite Black & Zeiss Zen lite Blue (https://www.zeiss.com/microscopy/int/products/microscope-software/zen-lite.html?vaURL=www.zeiss.com/zen-lite)

Heatmaps were generated by applying the following steps to each video:

1. Launch Icy and Open video.

Image/Sequence -> Open…

2. Choose the scene of interest.
3. Filter to remove noise

Processing -> Filtering -> Median filter (Input: Scene name, Type: 2D) -> Apply…

4. Export video for Zen formatting

Image/Sequence -> Rendering -> ARGB image…
Image/Sequence -> Save as (File type: AVI sequence)

5. Launch Zen black and Zen blue for Image Processing

Drag and drop exported video -> File -> Send to Zen- blue edition

6. Adjust histogram Intensity to the required preference for the channels
7. Dimension -> Drop down for Channel of interest -> LUT -> Rainbow
8. Export video with preferred dimension and frames/second

Processing ->Method -> Create Image Subset -> Parameters -> Select Channels, Time & Region of interest -> Apply
New window generates with applied settings -> Processing ->Method -> Movie Export -> Parameters -> Format (AVI uncompressed) -> Mapping (2.5fps) -> Apply

Quantification of SKL-labeled puncta

The areas of individual puncta and the average number of puncta per cell were calculated using the spots function of FIJI/imageJ software, applying the following steps to each image:

1 – Open image.
File -> Open…
2 – Filter to remove noise.
Process -> Filters -> Gaussian Blur…
3 – Subtract background.
Process -> Subtract Background…
(the box marked "Light Background" was unticked).
4 – Set measurements to use later for filtering the puncta.
Analyze -> Set Measurements …

Tick the boxes marked "Area" and "Shape Descriptors". Then click on the "OK" button.

In this step, manually set in FIJI measurements to use as ‘‘filter’’ later in the workflow [which features to include/exclude in the counting (area, shape descriptors, centroid, perimeter)].

5 – Threshold image.
Image -> Adjust -> Threshold…

Box labeled ‘‘Dark Background’’ is ticked. Adjust the sliders so that features are red-colored, but the rest of the image is not. Click ‘‘Apply’’ button. This will replace the grayscale image with an ‘‘8-bit binary image’’. All ‘‘red’’ pixels are converted to a value of ‘‘255’’, while all non-red pixels will be given a value of ‘‘0’’.

6 – Fill in any holes in the nuclei.
Process -> Binary -> Fill Holes
7 – Separate ‘‘Touching’’ puncta.
Process -> Binary -> Watershed
8 – Perform the analysis.
Analyze -> Analyze Particles…

In this dialogue box, the algorithm starts to include or exclude puncta based on their attributes. ‘‘Size’’ smaller than 1 square pixel. ‘‘Circularity’’ set range: 200-1.

Rack surface overtime
1) Channel2-Ch2: Thick the box: absolute intensity
2) Min = 441 at t 380